

Search for the supersymmetric partner of the top quark in $p\bar{p}$ collisions at $\sqrt{s} = 1.96$ TeV

T. Aaltonen,²² B. Álvarez González^{v,10} S. Amerio,⁴² D. Amidei,³³ A. Anastassov,³⁷ A. Annovi,¹⁸ J. Antos,¹³ G. Apollinari,¹⁶ J.A. Appel,¹⁶ A. Apresyan,⁴⁷ T. Arisawa,⁵⁶ A. Artikov,¹⁴ J. Asaadi,⁵² W. Ashmanskas,¹⁶ B. Auerbach,⁵⁹ A. Aurisano,⁵² F. Azfar,⁴¹ W. Badgett,¹⁶ A. Barbaro-Galtieri,²⁷ V.E. Barnes,⁴⁷ B.A. Barnett,²⁴ P. Barria^{ee,45} P. Bartos,¹³ M. Bauce^{cc,42} G. Bauer,³¹ F. Bedeschi,⁴⁵ D. Beecher,²⁹ S. Behari,²⁴ G. Bellettini^{dd,45} J. Bellinger,⁵⁸ D. Benjamin,¹⁵ A. Beretvas,¹⁶ A. Bhatti,⁴⁹ M. Binkley*,¹⁶ D. Bisello^{cc,42} I. Bizjak^{ii,29} K.R. Bland,⁵ C. Blocker,⁷ B. Blumenfeld,²⁴ A. Bocci,¹⁵ A. Bodek,⁴⁸ D. Bortoletto,⁴⁷ J. Boudreau,⁴⁶ A. Boveia,¹² B. Brau^{a,16} L. Brigliadori^{bb,6} A. Brisuda,¹³ C. Bromberg,³⁴ E. Brucken,²² M. Bucciantonio^{dd,45} J. Budagov,¹⁴ H.S. Budd,⁴⁸ S. Budd,²³ K. Burkett,¹⁶ G. Busetto^{cc,42} P. Bussey,²⁰ A. Buzatu,³² S. Cabrera^{x,15} C. Calancha,³⁰ S. Camarda,⁴ M. Campanelli,³⁴ M. Campbell,³³ F. Canelli^{12,16} A. Canepa,⁴⁴ B. Carls,²³ D. Carlsmith,⁵⁸ R. Carosi,⁴⁵ S. Carrillo^{k,17} S. Carron,¹⁶ B. Casal,¹⁰ M. Casarsa,¹⁶ A. Castro^{bb,6} P. Catastini,¹⁶ D. Cauz,⁵³ V. Cavaliere^{ee,45} M. Cavalli-Sforza,⁴ A. Cerri^{f,27} L. Cerrito^{q,29} Y.C. Chen,¹ M. Chertok,⁸ G. Chiarelli,⁴⁵ G. Chlachidze,¹⁶ F. Chlebana,¹⁶ K. Cho,²⁶ D. Chokheli,¹⁴ J.P. Chou,²¹ W.H. Chung,⁵⁸ Y.S. Chung,⁵⁸ C.I. Ciobanu,⁴³ M.A. Ciocci^{ee,45} A. Clark,¹⁹ D. Clark,⁷ G. Compostella^{cc,42} M.E. Convery,¹⁶ J. Conway,⁸ M. Corbo,⁴³ M. Cordelli,¹⁸ C.A. Cox,⁸ D.J. Cox,⁸ F. Crescioli^{dd,45} C. Cuenca Almenar,⁵⁹ J. Cuevas^{v,10} R. Culbertson,¹⁶ D. Dagenhart,¹⁶ N. d'Ascenzo^{t,43} M. Datta,¹⁶ P. de Barbaro,⁴⁸ S. De Cecco,⁵⁰ G. De Lorenzo,⁴ M. Dell'Orso^{dd,45} C. Deluca,⁴ L. Demortier,⁴⁹ J. Deng^{c,15} M. Deninno,⁶ F. Devoto,²² M. d'Errico^{cc,42} A. Di Canto^{dd,45} B. Di Ruzza,⁴⁵ J.R. Dittmann,⁵ M. D'Onofrio,²⁸ S. Donati^{dd,45} P. Dong,¹⁶ T. Dorigo,⁴² K. Ebina,⁵⁶ A. Elagin,⁵² A. Eppig,³³ R. Erbacher,⁸ D. Errede,²³ S. Errede,²³ N. Ershaidat^{aa,43} R. Eusebi,⁵² H.C. Fang,²⁷ S. Farrington,⁴¹ M. Feindt,²⁵ J.P. Fernandez,³⁰ C. Ferrazza^{ff,45} R. Field,¹⁷ G. Flanagan^{r,47} R. Forrest,⁸ M.J. Frank,⁵ M. Franklin,²¹ J.C. Freeman,¹⁶ I. Furic,¹⁷ M. Gallinaro,⁴⁹ J. Galyardt,¹¹ J.E. Garcia,¹⁹ A.F. Garfinkel,⁴⁷ P. Garosi^{ee,45} H. Gerberich,²³ E. Gerchtein,¹⁶ S. Giagu^{gg,50} V. Giakoumopoulou,³ P. Giannetti,⁴⁵ K. Gibson,⁴⁶ C.M. Ginsburg,¹⁶ N. Giokaris,³ P. Giomini,¹⁸ M. Giunta,⁴⁵ G. Giurgiu,²⁴ V. Glagolev,¹⁴ D. Glenzinski,¹⁶ M. Gold,³⁶ D. Goldin,⁵² N. Goldschmidt,¹⁷ A. Golossanov,¹⁶ G. Gomez,¹⁰ G. Gomez-Ceballos,³¹ M. Goncharov,³¹ O. González,³⁰ I. Gorelov,³⁶ A.T. Goshaw,¹⁵ K. Goulianos,⁴⁹ A. Gresele,⁴² S. Grinstein,⁴ C. Grosso-Pilcher,¹² R.C. Group,¹⁶ J. Guimaraes da Costa,²¹ Z. Gunay-Unalan,³⁴ C. Haber,²⁷ S.R. Hahn,¹⁶ E. Halkiadakis,⁵¹ A. Hamaguchi,⁴⁰ J.Y. Han,⁴⁸ F. Happacher,¹⁸ K. Hara,⁵⁴ D. Hare,⁵¹ M. Hare,⁵⁵ R.F. Harr,⁵⁷ K. Hatakeyama,⁵ C. Hays,⁴¹ M. Heck,²⁵ J. Heinrich,⁴⁴ M. Herndon,⁵⁸ S. Hewamanage,⁵ D. Hidas,⁵¹ A. Hocker,¹⁶ W. Hopkins^{g,16} D. Horn,²⁵ S. Hou,¹ R.E. Hughes,³⁸ M. Hurwitz,¹² U. Husemann,⁵⁹ N. Hussain,³² M. Hussein,³⁴ J. Huston,³⁴ G. Introzzi,⁴⁵ M. Iori^{gg,50} A. Ivanov^{o,8} E. James,¹⁶ D. Jang,¹¹ B. Jayatilaka,¹⁵ E.J. Jeon,²⁶ M.K. Jha,⁶ S. Jindariani,¹⁶ W. Johnson,⁸ M. Jones,⁴⁷ K.K. Joo,²⁶ S.Y. Jun,¹¹ T.R. Junk,¹⁶ T. Kamon,⁵² P.E. Karchin,⁵⁷ Y. Kato^{n,40} W. Ketchum,¹² J. Keung,⁴⁴ V. Khotilovich,⁵² B. Kilminster,¹⁶ D.H. Kim,²⁶ H.S. Kim,²⁶ H.W. Kim,²⁶ J.E. Kim,²⁶ M.J. Kim,¹⁸ S.B. Kim,²⁶ S.H. Kim,⁵⁴ Y.K. Kim,¹² N. Kimura,⁵⁶ S. Klimenko,¹⁷ K. Kondo,⁵⁶ D.J. Kong,²⁶ J. Konigsberg,¹⁷ A. Korytov,¹⁷ A.V. Kotwal,¹⁵ M. Kreps,²⁵ J. Kroll,⁴⁴ D. Krop,¹² N. Krumnack^{l,5} M. Kruse,¹⁵ V. Krutelyov^{d,52} T. Kuhr,²⁵ M. Kurata,⁵⁴ S. Kwang,¹² A.T. Laasanen,⁴⁷ S. Lami,⁴⁵ S. Lammel,¹⁶ M. Lancaster,²⁹ R.L. Lander,⁸ K. Lannon^{u,38} A. Lath,⁵¹ G. Latino^{ee,45} I. Lazzizzera,⁴² T. LeCompte,² E. Lee,⁵² H.S. Lee,¹² J.S. Lee,²⁶ S.W. Lee^{w,52} S. Leo^{dd,45} S. Leone,⁴⁵ J.D. Lewis,¹⁶ C.-J. Lin,²⁷ J. Linacre,⁴¹ M. Lindgren,¹⁶ E. Lipeles,⁴⁴ A. Lister,¹⁹ D.O. Litvintsev,¹⁶ C. Liu,⁴⁶ Q. Liu,⁴⁷ T. Liu,¹⁶ S. Lockwitz,⁵⁹ N.S. Lockyer,⁴⁴ A. Loginov,⁵⁹ D. Lucchesi^{cc,42} J. Lueck,²⁵ P. Lujan,²⁷ P. Lukens,¹⁶ G. Lungu,⁴⁹ J. Lys,²⁷ R. Lysak,¹³ R. Madrak,¹⁶ K. Maeshima,¹⁶ K. Makhoul,³¹ P. Maksimovic,²⁴ S. Malik,⁴⁹ G. Manca^{b,28} A. Manousakis-Katsikakis,³ F. Margaroli,⁴⁷ C. Marino,²⁵ M. Martínez,⁴ R. Martínez-Ballarín,³⁰ P. Mastrandrea,⁵⁰ M. Mathis,²⁴ M.E. Mattson,⁵⁷ P. Mazzanti,⁶ K.S. McFarland,⁴⁸ P. McIntyre,⁵² R. McNulty^{i,28} A. Mehta,²⁸ P. Mehtala,²² A. Menzione,⁴⁵ C. Mesropian,⁴⁹ T. Miao,¹⁶ D. Mietlicki,³³ A. Mitra,¹ H. Miyake,⁵⁴ S. Moed,²¹ N. Moggi,⁶ M.N. Mondragon^{k,16} C.S. Moon,²⁶ R. Moore,¹⁶ M.J. Morello,¹⁶ J. Morlock,²⁵ P. Movilla Fernandez,¹⁶ A. Mukherjee,¹⁶ Th. Muller,²⁵ P. Murat,¹⁶ M. Mussini^{bb,6} J. Nachtman^{m,16} Y. Nagai,⁵⁴ J. Naganoma,⁵⁶ I. Nakano,³⁹ A. Napier,⁵⁵ J. Nett,⁵⁸ C. Neu^{z,44} M.S. Neubauer,²³ J. Nielsen^{e,27} L. Nodulman,² O. Norriella,²³ E. Nurse,²⁹ L. Oakes,⁴¹ S.H. Oh,¹⁵ Y.D. Oh,²⁶ I. Oksuzian,¹⁷ T. Okusawa,⁴⁰ R. Orava,²² L. Ortolan,⁴ S. Pagan Griso^{cc,42} C. Pagliarone,⁵³ E. Palencia^{f,10} V. Papadimitriou,¹⁶ A.A. Paramonov,² J. Patrick,¹⁶ G. Pauletta^{hh,53} M. Paulini,¹¹ C. Paus,³¹ D.E. Pellett,⁸ A. Penzo,⁵³ T.J. Phillips,¹⁵ G. Piacentino,⁴⁵ E. Pianori,⁴⁴ J. Pilot,³⁸ K. Pitts,²³ C. Plager,⁹ L. Pondrom,⁵⁸ K. Potamianos,⁴⁷ O. Poukhov*,¹⁴ F. Prokoshin^{y,14} A. Pronko,¹⁶ F. Ptohos^{h,18} E. Pueschel,¹¹ G. Punzi^{dd,45} J. Pursley,⁵⁸ A. Rahaman,⁴⁶ V. Ramakrishnan,⁵⁸ N. Ranjan,⁴⁷ I. Redondo,³⁰ P. Renton,⁴¹ M. Rescigno,⁵⁰

F. Rimondi^{bb,6}, L. Ristori^{45,16}, A. Robson,²⁰ T. Rodrigo,¹⁰ T. Rodriguez,⁴⁴ E. Rogers,²³ S. Rolli,⁵⁵ R. Roser,¹⁶ M. Rossi,⁵³ F. Ruffini^{ee,45}, A. Ruiz,¹⁰ J. Russ,¹¹ V. Rusu,¹⁶ A. Safonov,⁵² W.K. Sakumoto,⁴⁸ L. Santi^{hh,53}, L. Sartori,⁴⁵ K. Sato,⁵⁴ V. Saveliev^{t,43}, A. Savoy-Navarro,⁴³ P. Schlabach,¹⁶ A. Schmidt,²⁵ E.E. Schmidt,¹⁶ M.P. Schmidt^{*,59}, M. Schmitt,³⁷ T. Schwarz,⁸ L. Scodellaro,¹⁰ A. Scribano^{ee,45}, F. Scuri,⁴⁵ A. Sedov,⁴⁷ S. Seidel,³⁶ Y. Seiya,⁴⁰ A. Semenov,¹⁴ F. Sforza^{dd,45}, A. Sfyrta,²³ S.Z. Shalhout,⁸ T. Shears,²⁸ P.F. Shepard,⁴⁶ M. Shimojima^{s,54}, S. Shiraishi,¹² M. Shochet,¹² I. Shreyber,³⁵ A. Simonenko,¹⁴ P. Sinervo,³² A. Sissakian^{*,14}, K. Sliwa,⁵⁵ J.R. Smith,⁸ F.D. Snider,¹⁶ A. Soha,¹⁶ S. Somalwar,⁵¹ V. Sorin,⁴ P. Squillacioti,¹⁶ M. Stanitzki,⁵⁹ R. St. Denis,²⁰ B. Stelzer,³² O. Stelzer-Chilton,³² D. Stentz,³⁷ J. Strologas,³⁶ G.L. Strycker,³³ Y. Sudo,⁵⁴ A. Sukhanov,¹⁷ I. Suslov,¹⁴ K. Takemasa,⁵⁴ Y. Takeuchi,⁵⁴ J. Tang,¹² M. Tecchio,³³ P.K. Teng,¹ J. Thom^{g,16}, J. Thome,¹¹ G.A. Thompson,²³ E. Thomson,⁴⁴ P. Ttito-Guzmán,³⁰ S. Tkaczyk,¹⁶ D. Toback,⁵² S. Tokar,¹³ K. Tollefson,³⁴ T. Tomura,⁵⁴ D. Tonelli,¹⁶ S. Torre,¹⁸ D. Torretta,¹⁶ P. Totaro^{hh,53}, M. Trovato^{ff,45}, Y. Tu,⁴⁴ N. Turini^{ee,45}, F. Ukegawa,⁵⁴ S. Uozumi,²⁶ A. Varganov,³³ E. Vataga^{ff,45}, F. Vázquez^{k,17}, G. Velev,¹⁶ C. Vellidis,³ M. Vidal,³⁰ I. Vila,¹⁰ R. Vilar,¹⁰ M. Vogel,³⁶ G. Volpi^{dd,45}, P. Wagner,⁴⁴ R.L. Wagner,¹⁶ T. Wakisaka,⁴⁰ R. Wallny,⁹ S.M. Wang,¹ A. Warburton,³² D. Waters,²⁹ M. Weinberger,⁵² W.C. Wester III,¹⁶ B. Whitehouse,⁵⁵ D. Whiteson^{c,44}, A.B. Wicklund,² E. Wicklund,¹⁶ S. Wilbur,¹² F. Wick,²⁵ H.H. Williams,⁴⁴ J.S. Wilson,³⁸ P. Wilson,¹⁶ B.L. Winer,³⁸ P. Wittich^{g,16}, S. Wolbers,¹⁶ H. Wolfe,³⁸ T. Wright,³³ X. Wu,¹⁹ Z. Wu,⁵ K. Yamamoto,⁴⁰ J. Yamaoka,¹⁵ T. Yang,¹⁶ U.K. Yang^{p,12}, Y.C. Yang,²⁶ W.-M. Yao,²⁷ G.P. Yeh,¹⁶ K. Yi^{m,16}, J. Yoh,¹⁶ K. Yorita,⁵⁶ T. Yoshida^{j,40}, G.B. Yu,¹⁵ I. Yu,²⁶ S.S. Yu,¹⁶ J.C. Yun,¹⁶ A. Zanetti,⁵³ Y. Zeng,¹⁵ and S. Zucchelli^{bb6}

(CDF Collaboration[†])

¹*Institute of Physics, Academia Sinica, Taipei, Taiwan 11529, Republic of China*

²*Argonne National Laboratory, Argonne, Illinois 60439, USA*

³*University of Athens, 157 71 Athens, Greece*

⁴*Institut de Fisica d'Altes Energies, Universitat Autònoma de Barcelona, E-08193, Bellaterra (Barcelona), Spain*

⁵*Baylor University, Waco, Texas 76798, USA*

⁶*Istituto Nazionale di Fisica Nucleare Bologna, ^{bb}University of Bologna, I-40127 Bologna, Italy*

⁷*Brandeis University, Waltham, Massachusetts 02254, USA*

⁸*University of California, Davis, Davis, California 95616, USA*

⁹*University of California, Los Angeles, Los Angeles, California 90024, USA*

¹⁰*Instituto de Fisica de Cantabria, CSIC-University of Cantabria, 39005 Santander, Spain*

¹¹*Carnegie Mellon University, Pittsburgh, Pennsylvania 15213, USA*

¹²*Enrico Fermi Institute, University of Chicago, Chicago, Illinois 60637, USA*

¹³*Comenius University, 842 48 Bratislava, Slovakia; Institute of Experimental Physics, 040 01 Kosice, Slovakia*

¹⁴*Joint Institute for Nuclear Research, RU-141980 Dubna, Russia*

¹⁵*Duke University, Durham, North Carolina 27708, USA*

¹⁶*Fermi National Accelerator Laboratory, Batavia, Illinois 60510, USA*

¹⁷*University of Florida, Gainesville, Florida 32611, USA*

¹⁸*Laboratori Nazionali di Frascati, Istituto Nazionale di Fisica Nucleare, I-00044 Frascati, Italy*

¹⁹*University of Geneva, CH-1211 Geneva 4, Switzerland*

²⁰*Glasgow University, Glasgow G12 8QQ, United Kingdom*

²¹*Harvard University, Cambridge, Massachusetts 02138, USA*

²²*Division of High Energy Physics, Department of Physics,*

University of Helsinki and Helsinki Institute of Physics, FIN-00014, Helsinki, Finland

²³*University of Illinois, Urbana, Illinois 61801, USA*

²⁴*The Johns Hopkins University, Baltimore, Maryland 21218, USA*

²⁵*Institut für Experimentelle Kernphysik, Karlsruhe Institute of Technology, D-76131 Karlsruhe, Germany*

²⁶*Center for High Energy Physics: Kyungpook National University,*

Daegu 702-701, Korea; Seoul National University, Seoul 151-742,

Korea; Sungkyunkwan University, Suwon 440-746,

Korea; Korea Institute of Science and Technology Information,

Daejeon 305-806, Korea; Chonnam National University, Gwangju 500-757,

Korea; Chonbuk National University, Jeonju 561-756, Korea

²⁷*Ernest Orlando Lawrence Berkeley National Laboratory, Berkeley, California 94720, USA*

²⁸*University of Liverpool, Liverpool L69 7ZE, United Kingdom*

²⁹*University College London, London WC1E 6BT, United Kingdom*

³⁰*Centro de Investigaciones Energeticas Medioambientales y Tecnológicas, E-28040 Madrid, Spain*

³¹*Massachusetts Institute of Technology, Cambridge, Massachusetts 02139, USA*

³²*Institute of Particle Physics: McGill University, Montréal, Québec,*

Canada H3A 2T8; Simon Fraser University, Burnaby, British Columbia,

Canada V5A 1S6; University of Toronto, Toronto, Ontario,

Canada M5S 1A7; and TRIUMF, Vancouver, British Columbia, Canada V6T 2A3

- ³³University of Michigan, Ann Arbor, Michigan 48109, USA
³⁴Michigan State University, East Lansing, Michigan 48824, USA
³⁵Institution for Theoretical and Experimental Physics, ITEP, Moscow 117259, Russia
³⁶University of New Mexico, Albuquerque, New Mexico 87131, USA
³⁷Northwestern University, Evanston, Illinois 60208, USA
³⁸The Ohio State University, Columbus, Ohio 43210, USA
³⁹Okayama University, Okayama 700-8530, Japan
⁴⁰Osaka City University, Osaka 588, Japan
⁴¹University of Oxford, Oxford OX1 3RH, United Kingdom
⁴²Istituto Nazionale di Fisica Nucleare, Sezione di Padova-Trento, ^{cc}University of Padova, I-35131 Padova, Italy
⁴³LPNHE, Universite Pierre et Marie Curie/IN2P3-CNRS, UMR7585, Paris, F-75252 France
⁴⁴University of Pennsylvania, Philadelphia, Pennsylvania 19104, USA
⁴⁵Istituto Nazionale di Fisica Nucleare Pisa, ^{dd}University of Pisa, Italy
^{ee}University of Siena and ^{ff}Scuola Normale Superiore, I-56127 Pisa, Italy
⁴⁶University of Pittsburgh, Pittsburgh, Pennsylvania 15260, USA
⁴⁷Purdue University, West Lafayette, Indiana 47907, USA
⁴⁸University of Rochester, Rochester, New York 14627, USA
⁴⁹The Rockefeller University, New York, New York 10065, USA
⁵⁰Istituto Nazionale di Fisica Nucleare, Sezione di Roma 1,
^{gg}Sapienza Università di Roma, I-00185 Roma, Italy
⁵¹Rutgers University, Piscataway, New Jersey 08855, USA
⁵²Texas A&M University, College Station, Texas 77843, USA
⁵³Istituto Nazionale di Fisica Nucleare Trieste/Udine,
I-34100 Trieste, ^{hh}University of Trieste/Udine, I-33100 Udine, Italy
⁵⁴University of Tsukuba, Tsukuba, Ibaraki 305, Japan
⁵⁵Tufts University, Medford, Massachusetts 02155, USA
⁵⁶Waseda University, Tokyo 169, Japan
⁵⁷Wayne State University, Detroit, Michigan 48201, USA
⁵⁸University of Wisconsin, Madison, Wisconsin 53706, USA
⁵⁹Yale University, New Haven, Connecticut 06520, USA
- (Dated: November 8, 2021)

We present a search for the lightest supersymmetric partner of the top quark in proton-antiproton collisions at a center-of-mass energy $\sqrt{s} = 1.96$ TeV. This search was conducted within the framework of the R -parity conserving minimal supersymmetric extension of the standard model, assuming the stop decays dominantly to a lepton, a sneutrino, and a bottom quark. We searched for events with two oppositely-charged leptons, at least one jet, and missing transverse energy in a data sample corresponding to an integrated luminosity of 1 fb^{-1} collected by the CDF experiment. No significant evidence of a stop quark signal was found. Exclusion limits at 95% confidence level in the stop quark versus sneutrino mass plane are set. Stop quark masses up to $180 \text{ GeV}/c^2$ are excluded for sneutrino masses around $45 \text{ GeV}/c^2$, and sneutrino masses up to $116 \text{ GeV}/c^2$ are excluded for stop quark masses around $150 \text{ GeV}/c^2$.

PACS numbers: 14.80.Ly, 13.85.Rm, 12.60.Jv

I. INTRODUCTION

The minimal supersymmetric standard model [1] (MSSM) was introduced to solve several problems that arise in the standard model (SM). These include: the

*Deceased

†With visitors from ^aUniversity of Massachusetts Amherst, Amherst, Massachusetts 01003, ^bIstituto Nazionale di Fisica Nucleare, Sezione di Cagliari, 09042 Monserrato (Cagliari), Italy, ^cUniversity of California Irvine, Irvine, CA 92697, ^dUniversity of California Santa Barbara, Santa Barbara, CA 93106 ^eUniversity of California Santa Cruz, Santa Cruz, CA 95064, ^fCERN, CH-1211 Geneva, Switzerland, ^gCornell University, Ithaca, NY 14853, ^hUniversity of Cyprus, Nicosia CY-1678, Cyprus, ⁱUniversity College Dublin, Dublin 4, Ireland, ^jUniversity of Fukui, Fukui City, Fukui Prefecture, Japan 910-0017, ^kUniversidad Iberoamericana, Mexico D.F., Mexico, ^lIowa State University, Ames, IA 50011, ^mUniversity of Iowa, Iowa City, IA 52242, ⁿKinki University, Higashi-Osaka City, Japan 577-8502, ^oKansas State University, Manhattan, KS 66506, ^pUniversity of Manchester, Manchester M13 9PL, England, ^qQueen Mary, University of London, London, E1

⁴NS, England, ^rMuons, Inc., Batavia, IL 60510, ^sNagasaki Institute of Applied Science, Nagasaki, Japan, ^tNational Research Nuclear University, Moscow, Russia, ^uUniversity of Notre Dame, Notre Dame, IN 46556, ^vUniversidad de Oviedo, E-33007 Oviedo, Spain, ^wTexas Tech University, Lubbock, TX 79609, ^xIFIC(CSIC-Universitat de Valencia), 56071 Valencia, Spain, ^yUniversidad Tecnica Federico Santa Maria, 110v Valparaiso, Chile, ^zUniversity of Virginia, Charlottesville, VA 22906, ^{aa}Yarmouk University, Irbid 211-63, Jordan, ⁱⁱOn leave from J. Stefan Institute, Ljubljana, Slovenia,

hierarchy problem that requires the fine-tuning of theoretical parameters in order to obtain cancellation of large quantum corrections to the Higgs mass; the lack of convergence of the strong, weak, and electromagnetic gauge couplings at the grand-unification energy scale; and the lack of a dark matter candidate.

The MSSM assigns a new bosonic counterpart to each SM fermion and likewise a fermionic superpartner to each SM boson. This results in scalar partners \tilde{q}_L and \tilde{q}_R to the SM quark helicity states q_L and q_R . There can be two supersymmetric mass eigenstates for each supersymmetric quark (squark) corresponding to the two fermionic degrees-of-freedom of the SM quark. The supersymmetric scalar top quark (stop) mass eigenstates \tilde{t}_1 and \tilde{t}_2 are rotated relative to \tilde{t}_L and \tilde{t}_R by a mixing angle $\theta_{\tilde{t}}$. In some models [2], $m_{\tilde{t}_{1,2}} \approx m_t$. The large mass of the top quark and the corresponding large value of the top-to-Higgs coupling constant may lead to a large splitting between $m_{\tilde{t}_1}$ and $m_{\tilde{t}_2}$. Consequently the lower mass stop quark eigenstate is expected to be the lightest of all the squarks, with a mass even below the top quark, making its detection at the Tevatron a realistic possibility.

The MSSM possesses a new conserved quantity called R -parity (R_p), defined as $R_p = (-1)^{3(B-L)+2S}$, where B is the baryon number, L is the lepton number, and S is the spin. As a consequence, the lightest supersymmetric particle (LSP) must be stable, and is a dark matter candidate. Because the initial state of $p\bar{p}$ collisions has $R_p = +1$ and supersymmetric particles have $R_p = -1$, supersymmetric particles must be pair-produced. At the Tevatron stop quarks are expected to be produced primarily through gluon-gluon (gg) fusion and quark-antiquark ($q\bar{q}$) annihilation, with gg fusion dominant at low stop masses ($< 100 \text{ GeV}/c^2$) and $q\bar{q}$ annihilation dominant at higher stop masses [3].

The produced stop (\tilde{t}) quarks can decay via several possible channels, depending on the masses of the particles involved. Two-body decays include $\tilde{t} \rightarrow t\tilde{\chi}_1^0$, $\tilde{t} \rightarrow b\tilde{\chi}_1^+$, and $\tilde{t} \rightarrow c\tilde{\chi}_1^0$ where $\tilde{\chi}_1^0$ is the lightest neutralino and $\tilde{\chi}_1^+$ the lightest chargino. These decays may not be kinematically possible for a light stop or they may be suppressed by higher order diagrams. They are also constrained by existing limits [4, 5]. Possible three-body decays include $\tilde{t} \rightarrow W^+b\tilde{\chi}_1^0$, $\tilde{t} \rightarrow b\tilde{l}^+\nu_l$, and $\tilde{t} \rightarrow bl^+\tilde{\nu}_l$ where \tilde{l} is the supersymmetric lepton and $\tilde{\nu}_l$ the supersymmetric neutrino. Limits on the supersymmetric lepton and neutralino masses from experiments at the large electron-positron collider (LEP) [4] restrict the range of stop masses available to the first two decay modes.

The decay $\tilde{t} \rightarrow bl^+\tilde{\nu}_l$, which proceeds via a virtual chargino, is the subject of this analysis. We assume the branching ratio for this decay mode is 100% and that electrons, muons, and taus are equally likely decay products. While electrons and muons are detected directly, taus are only included opportunistically in this analysis through their decays into electrons and muons. We also assume that the supersymmetric neutrino decays neutrally into the LSP (or is the LSP), thus escaping unde-

tected and leading to missing transverse energy (\cancel{E}_T) [6] in the detector. Since stop quarks are produced in pairs, we search for events with two opposite-charge leptons (ee , $e\mu$, $\mu\mu$), \cancel{E}_T , and at least one hadronic jet.

Previous searches at LEP and at the Tevatron [4, 5] for the stop quark using the same topology as this analysis have produced negative results. These analyses have set 95% confidence level exclusion limits in the stop-sneutrino mass plane. This paper extends the earlier CDF results based on 107 pb^{-1} of data at $\sqrt{s} = 1.8 \text{ TeV}$ to 1 fb^{-1} at $\sqrt{s} = 1.96 \text{ TeV}$.

The structure of this paper is as follows: Section II details the detector and the data set; Sections III describes the background estimation; Section IV the signal predictions and systematic uncertainties; Section V event pre-selection and control samples; Section VI explains the optimization of event selection cuts; and Section VII presents the results and conclusions.

II. THE DETECTOR AND DATA SET

The data sample corresponds to an integrated luminosity of 1 fb^{-1} of $p\bar{p}$ collisions at a center-of-mass energy of 1.96 TeV collected with the CDF detector [7] at the Fermilab Tevatron. Of particular relevance to this analysis are the tracking system, the calorimetry, and the muon detectors.

The tracking system consists of two silicon micro-strip detectors and a multi-wire open-cell drift chamber, the central outer tracker (COT). The silicon vertex detector (SVX) and the intermediate silicon layers cover the pseudorapidity [6] region $|\eta| < 2$ while the COT covers $|\eta| < 1$. The tracking system is surrounded by a superconducting solenoid with a magnetic field of 1.4 T . The relative track momentum resolution provided by the COT is $\sigma_{p_T}/p_T^2 \simeq 0.0015(\text{GeV}/c)^{-1}$.

Outside the magnet in the radial direction are electromagnetic and hadronic calorimeters arranged in a projective tower geometry with a tower granularity of $\Delta\eta \times \Delta\phi \simeq 0.1 \times 0.26$ in the central region. The central electromagnetic calorimeter (CEM) utilizes lead-scintillator sampling and covers $|\eta| < 1.1$, with energy resolution for electrons $\sigma_{E_T}/E_T \simeq 13.5\%/\sqrt{E_T}(\text{GeV}) \oplus 2\%$. The central electromagnetic shower maximum detector (CES) is located inside the CEM at a depth of six radiation lengths, close to the position of maximum electromagnetic shower development, and is used for the determination of the shower shape and for matching the shower location to the track extrapolation. The central hadron calorimeter (CHA) uses iron-scintillator sampling and covers $|\eta| < 0.9$. Its energy resolution for hadrons is $\sigma_{E_T}/E_T \simeq 75\%/\sqrt{E_T}(\text{GeV}) \oplus 3\%$.

Additional calorimetry extends the coverage in the forward direction and is used in this analysis for calculating \cancel{E}_T and jet energies but not for lepton identification. The plug electromagnetic calorimeter covers $1.1 < |\eta| < 3.6$ and is constructed of lead and scintil-

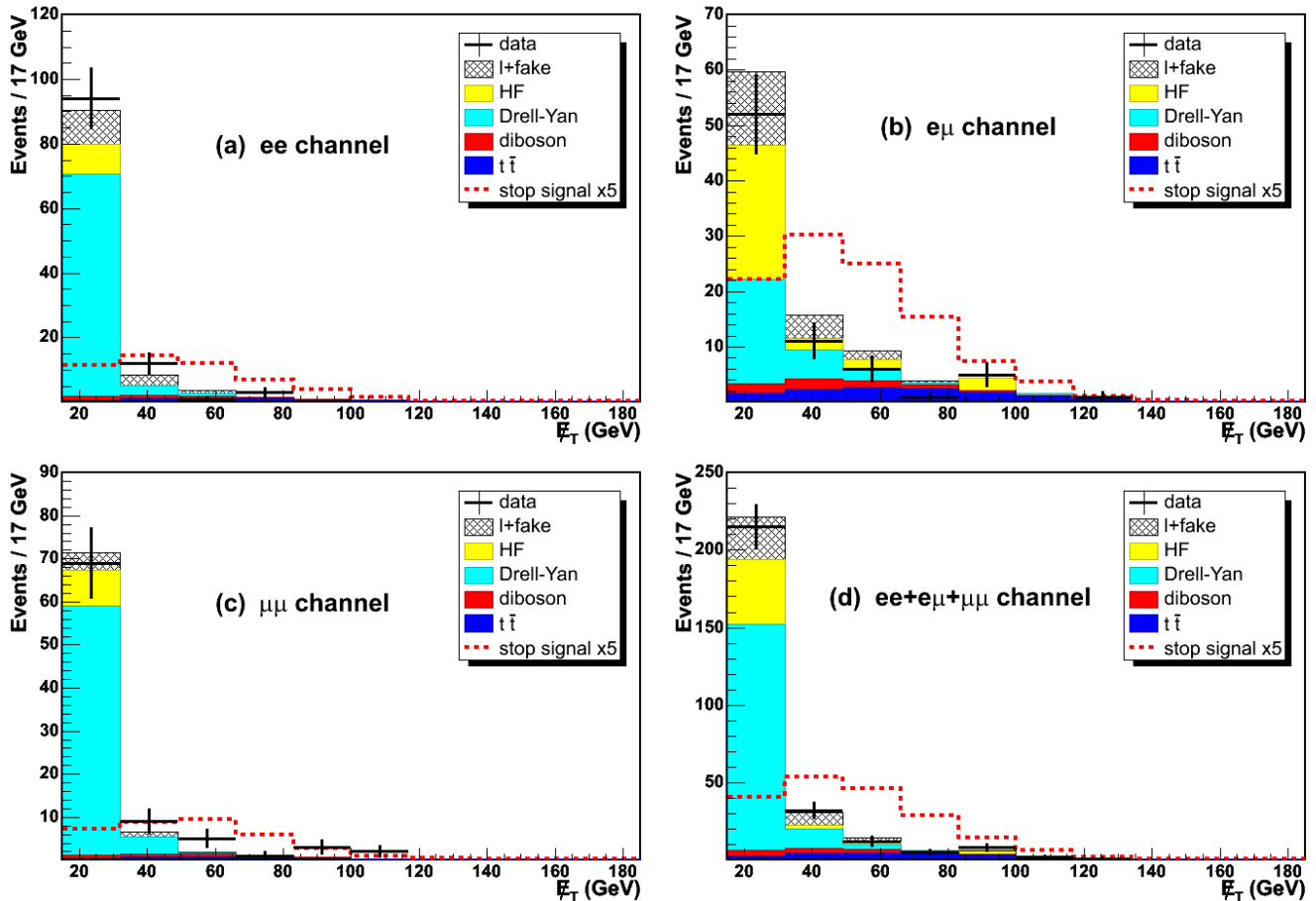


FIG. 1: \cancel{E}_T distributions in the pre-signal region for (a) the ee channel, (b) the $e\mu$ channel, (c) the $\mu\mu$ channel, and (d) the three channels combined. Data are shown as the points with error bars (statistical only). Shown as stacked histograms are the backgrounds arising from misidentified hadrons and decays-in-flight (l +fake), $b\bar{b}$ and $c\bar{c}$ (HF), DY, dibosons, and $t\bar{t}$. For reference, the expected signal for $(m_{\tilde{t}}, m_{\tilde{\nu}}) = (150, 75)$ GeV/c^2 , multiplied by five, is shown as the dashed line.

lator layers with an energy resolution for electrons of $\sigma_{E_T}/E_T \simeq 16\%/\sqrt{E_T} (\text{GeV}) \oplus 1\%$. The plug hadron calorimeter covers $1.3 < |\eta| < 3.6$ and is constructed of iron and scintillator layers with an energy resolution for hadrons of $\sigma_{E_T}/E_T \simeq 80\%/\sqrt{E_T} (\text{GeV}) \oplus 5\%$. The iron and scintillator wall hadron calorimeter covers the intermediate region $0.7 < |\eta| < 1.3$ between the central and plug hadron calorimeters. Its energy resolution is $\sigma_{E_T}/E_T \simeq 75\%/\sqrt{E_T} (\text{GeV}) \oplus 4\%$.

Radially outside the calorimetry is the muon detection system. The parts of the muon detector relevant to this analysis are the central muon detector (CMU), the central muon upgrade detector (CMP) and the central muon extension (CMX). The CMU consists of four-layer drift chambers and covers the pseudorapidity range $|\eta| < 0.6$. The CMP is made of four layers of single-wire drift cells located behind an additional 3.3 interaction lengths of steel and covers $|\eta| < 0.6$. Muons with reconstructed track stubs found in both the CMU and CMP are labeled CMUP muons. The CMX extends the coverage to $|\eta| < 1$ and is made up of eight layers of drift tubes.

The data were collected using a three-level trigger system. The first two levels are mostly hardware-based while the third level is software-based and is a fast version of the offline event reconstruction package. The online selection requires at least two lepton candidates falling into the following categories: CEM-CEM, CEM-CMUP, CEM-CMX, CMUP-CMUP, and CMUP-CMX, where the leptons are labeled by the detector components used in their identification. The triggers used in this analysis had an E_T threshold of 4 GeV for electrons and a p_T threshold of 4 GeV/c for muons.

All lepton candidates require the presence of a well-reconstructed track in the COT detector. Offline, electrons are required to pass a χ^2 comparison of the CES lateral shower profile in the $r-z$ view and the profile extracted from electron test-beam data. The shower position in the CES must also match the extrapolated position of the track. In addition, the lateral shower profile in the CEM towers must be consistent with that expected from test-beam data. The energy deposited in the calorimeters must be consistent with the track mo-

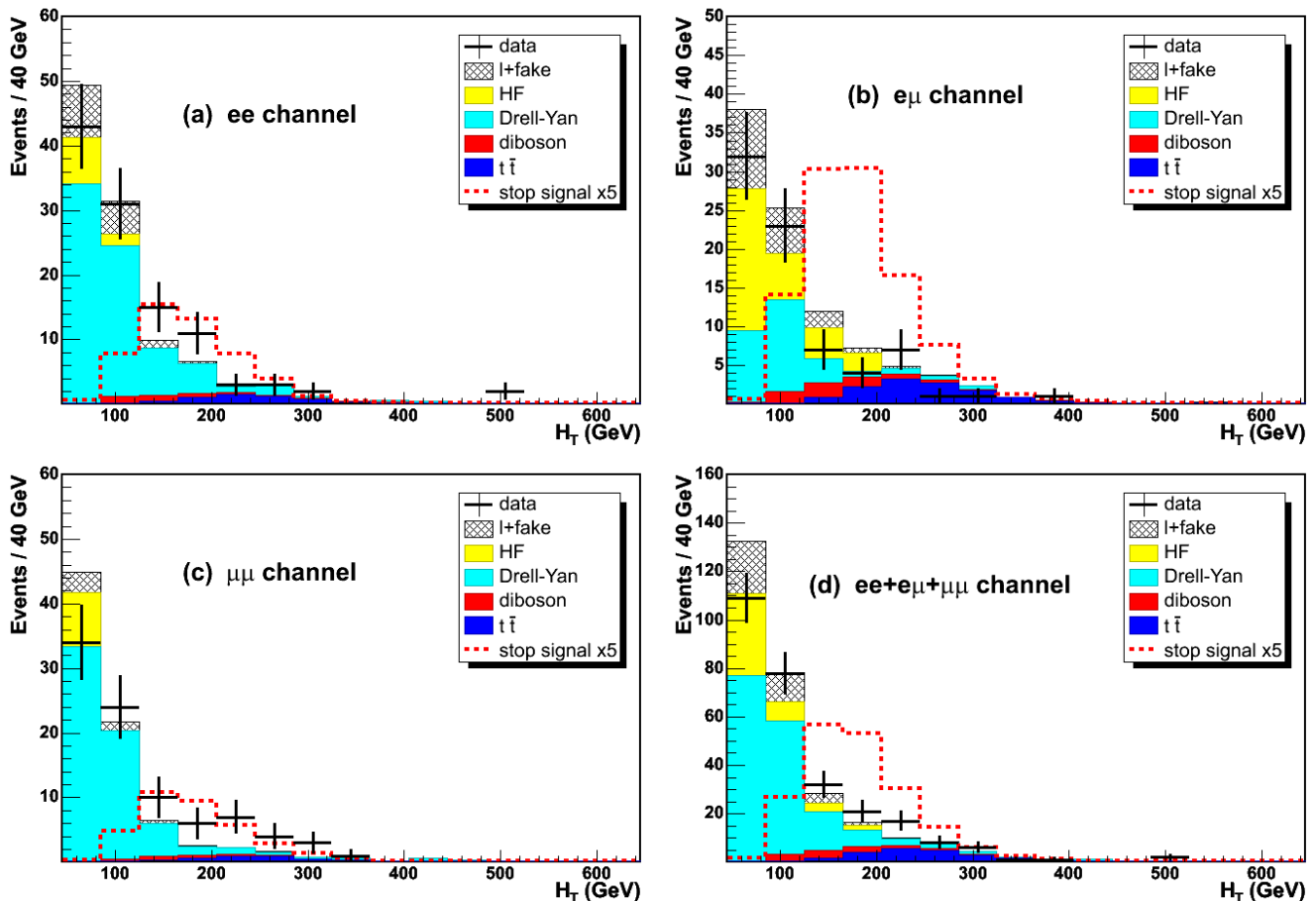


FIG. 2: H_T distributions in the pre-signal region, shown as in Fig. 1.

mentum measurement and the energy deposition in the CHA must be small. To reduce the background arising from the decay of hadrons in jets, the electrons are required to be isolated. Isolated electrons are selected by requiring that the remaining transverse energy after subtracting the transverse energy associated with the electron in a cone of 0.4 in $\eta - \phi$ space (E_T^{iso}) must be less than 2 GeV if $E_T \leq 20$ GeV or E_T^{iso}/E_T be less than 0.1 if $E_T > 20$ GeV. Electrons arising from photons that convert into e^+e^- pairs are removed by cuts applied to pairs of opposite-charge tracks with small opening angles. The electron identification efficiency was measured with Drell-Yan (DY) electrons to range from 75 to 83% [8] increasing with the electron E_T .

Muons are identified by matching tracks with reconstructed track stubs in the CMUP or CMX. The energy deposited in the calorimeters must be consistent with a minimum-ionizing particle. The isolation requirement is similar to that for electrons: $E_T^{iso} < 2$ GeV if $p_T \leq 20$ GeV/c or $E_T^{iso}/E_T < 0.1$ if $p_T > 20$ GeV/c. The muon identification efficiency was measured with J/ψ and Z data to be in the range 90 – 96% [8] rising with the muon p_T .

For both electrons and muons the impact parameter

(d_0) of the track with respect to the beam line position must be less than 0.2 cm if the track is based on COT information only or less than 0.02 cm if silicon-based tracking is also available. The longitudinal position of the event vertex is required to be within 60 cm of the center of the detector.

Jets are identified in $\eta - \phi$ space as a group of electromagnetic and hadronic towers using a clustering algorithm with cone size $\Delta R = \sqrt{(\Delta\eta)^2 + (\Delta\phi)^2} = 0.7$. The jet energy resolution is $\sigma \simeq 0.1 \cdot E_T$ (GeV) \oplus 1 GeV for jets with $35 < E_T < 450$ GeV. In order to find genuine hadronic jets and to avoid counting electrons and photons as jets, the fraction of the total energy deposited in the electromagnetic calorimeters is required to be between 0.1 and 0.9. Corrections to the jet energy are applied to take into account η -dependent losses, luminosity-dependent multiple interactions, and non-linearities in calorimeter response [9]. In this analysis we require at least one jet with $|\eta| < 2$ and $E_T > 15$ GeV after corrections.

\cancel{E}_T is calculated as the magnitude of the negative vector sum of the transverse energy deposited in the calorimeter towers with $|\eta| < 3.6$ and energy larger than 0.1 GeV. Since muons are minimum-ionizing particles

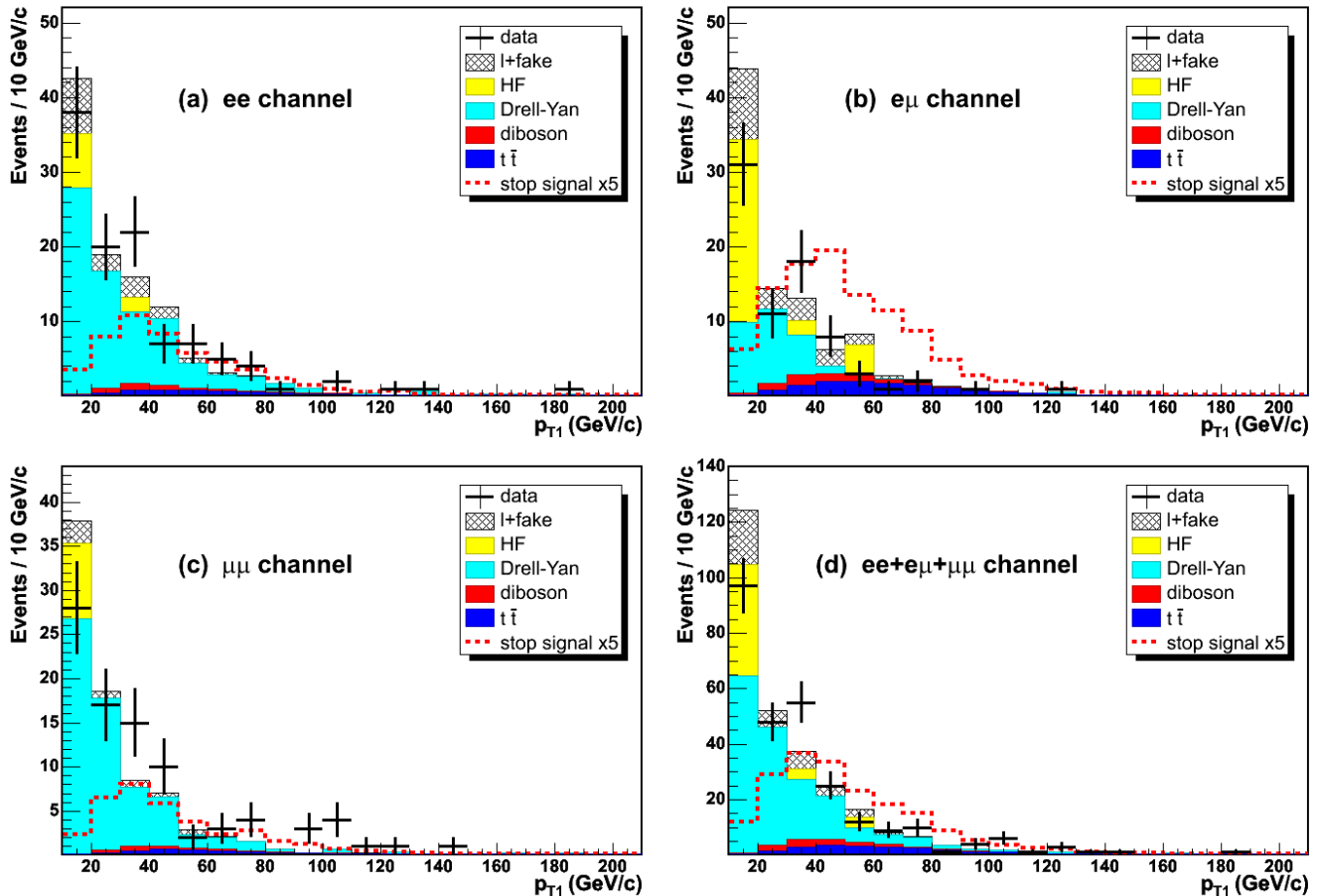


FIG. 3: p_T distributions of the highest p_T lepton in the pre-signal region, shown as in Fig. 1.

and deposit only $\simeq 2$ GeV energy in the calorimetry, the muon momentum from tracking (minus the expected energy deposition) is used to correct \cancel{E}_T . The energy corrections applied to jets with $|\eta| < 2.4$ and $E_T > 10$ GeV are also propagated to the calculation of \cancel{E}_T .

III. BACKGROUND ESTIMATION

Several background sources result in events with dileptons, jets, and \cancel{E}_T . These backgrounds are $t\bar{t}$ production, other heavy-flavor quark ($b\bar{b}$ and $c\bar{c}$) production, DY production of lepton pairs where mismeasurement of a jet or lepton results in substantial \cancel{E}_T , diboson production (WW , WZ , ZZ , and $W\gamma$), and events with a lepton and a misidentified or secondary lepton (l +fake). The jets in most backgrounds result from QCD initial-state or final-state radiation (ISR or FSR).

The $t\bar{t}$, DY, and diboson backgrounds are estimated by generating Monte Carlo (MC) events using the PYTHIA [10] event generator followed by a GEANT-based [11] detector simulation. Backgrounds arising from fake leptons and heavy flavor ($b\bar{b}$, $c\bar{c}$) are estimated using data-driven methods.

The MC $t\bar{t}$ samples are normalized to the next-to-leading-order (NLO) cross section $\sigma_{t\bar{t}} = 6.71$ pb [12] with a top mass of 175 GeV/c^2 . The $Z \rightarrow ee$, $Z \rightarrow \mu\mu$, and $Z \rightarrow \tau\tau$ samples are normalized to a leading-order cross section times branching ratio of 1272 pb for $m_{ll} > 10$ GeV/c^2 times a k -factor of 1.4 [13] to correct for NLO contributions. The NLO cross sections times branching ratios for $WW \rightarrow ll\nu\nu$, $WZ \rightarrow llX$, and $ZZ \rightarrow llX$ are 1.27 , 0.365 , and 1.513 pb respectively [14]. For $W\gamma \rightarrow e\nu\gamma$ and $W\gamma \rightarrow \mu\nu\gamma$, we use the leading order cross section of 21.5 pb times a k -factor of 1.34 to account for NLO contributions [15].

The lepton plus fake background consists of events with a genuine lepton plus a “fake” lepton which is either a light hadron misidentified as a lepton or an uninteresting lepton from pion or kaon decay-in-flight. For muons the fakes can be particles that penetrate the calorimeters and absorbing material and reach the muon detectors or decay in flight to muons. In the case of electrons, fakes are usually jets that are misidentified as electrons, mainly due to neutral pions that decay to photons which shower in the electromagnetic calorimeters. This background is estimated by examining samples of single-lepton events taken with the $E_T > 8$ GeV electron calibration trigger

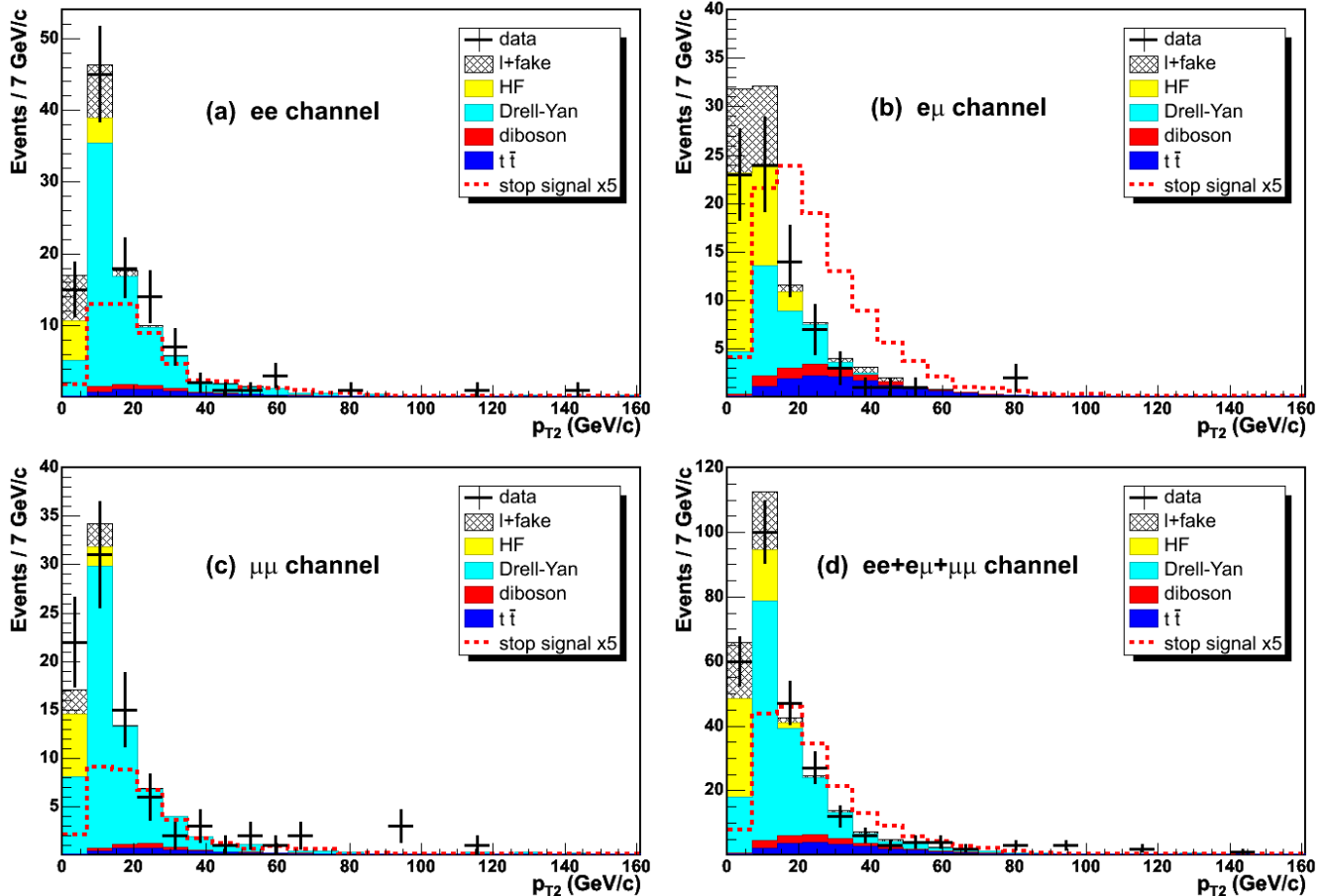


FIG. 4: p_T distributions of the next-to-highest p_T lepton in the pre-signal region, shown as in Fig. 1.

and the $p_T > 8$ GeV/ c muon calibration trigger. Events with at least one $E_T > 4$ GeV central jet ($|\eta| < 1.1$) or one isolated track with $p_T > 4$ GeV/ c passing the muon track quality cuts, excluding the trigger lepton, form the l +fake-electron and l +fake-muon candidate samples, respectively. To determine the background, it is necessary to estimate a fake rate from samples of jet events that contain a negligible number of directly produced leptons. Four samples containing jets with $E_T > 20, 50, 70,$ and 100 GeV, respectively, are used. The electron fake rate is defined as the probability of a jet being misidentified as an electron and the muon fake rate as the probability of an isolated track being misidentified as a muon. The fake rates are determined as a function of jet E_T for electrons and of track p_T for muons. The fake rate for 20 GeV electrons is about 0.0002 fakes per jet and the fake rate for 20 GeV/ c muons is about 0.004 fakes per track. These fake rates are then applied to each fake-electron and fake-muon candidate, one at a time, in the single lepton sample. Events that pass the analysis cuts are assigned a weight, which is the appropriate fake rate, scaled to the integrated luminosity of the dilepton data sample relative to the integrated luminosity of the single lepton sample, taking into account the single lep-

ton trigger prescale. The sum of the weights then forms the l +fake background. A 50% systematic uncertainty on the misidentified lepton background is assigned based upon the differences between the four jet samples used to determine the fake rates.

The background arising from heavy-flavor ($b\bar{b}, c\bar{c}$) is estimated utilizing dilepton events enriched in heavy-flavor events by inverting the normal impact parameter requirements, i.e. $|d_0| > 0.2$ cm for COT-only tracks and $|d_0| > 0.02$ cm if the track included information from the SVX, and requiring that at least one lepton pass the inverse d_0 cuts. A “scaling region” is defined as the dilepton invariant mass range $15 < M_{ll} < 35$ GeV/ c^2 . The scaling region has no requirements on \cancel{E}_T , the number of jets, or other kinematic variables. In this region the only significant contributions to the data sample with normal d_0 cuts are due to DY, heavy-flavor, and light hadrons misidentified as leptons. The DY contribution is derived from MC samples, and the misidentified lepton component is estimated using the technique described above. The remaining events are attributed to heavy-flavor (HF) and are used to calculate scaling factors, defined as the ratio of these inferred HF events passing the normal d_0 cuts to the total number of events

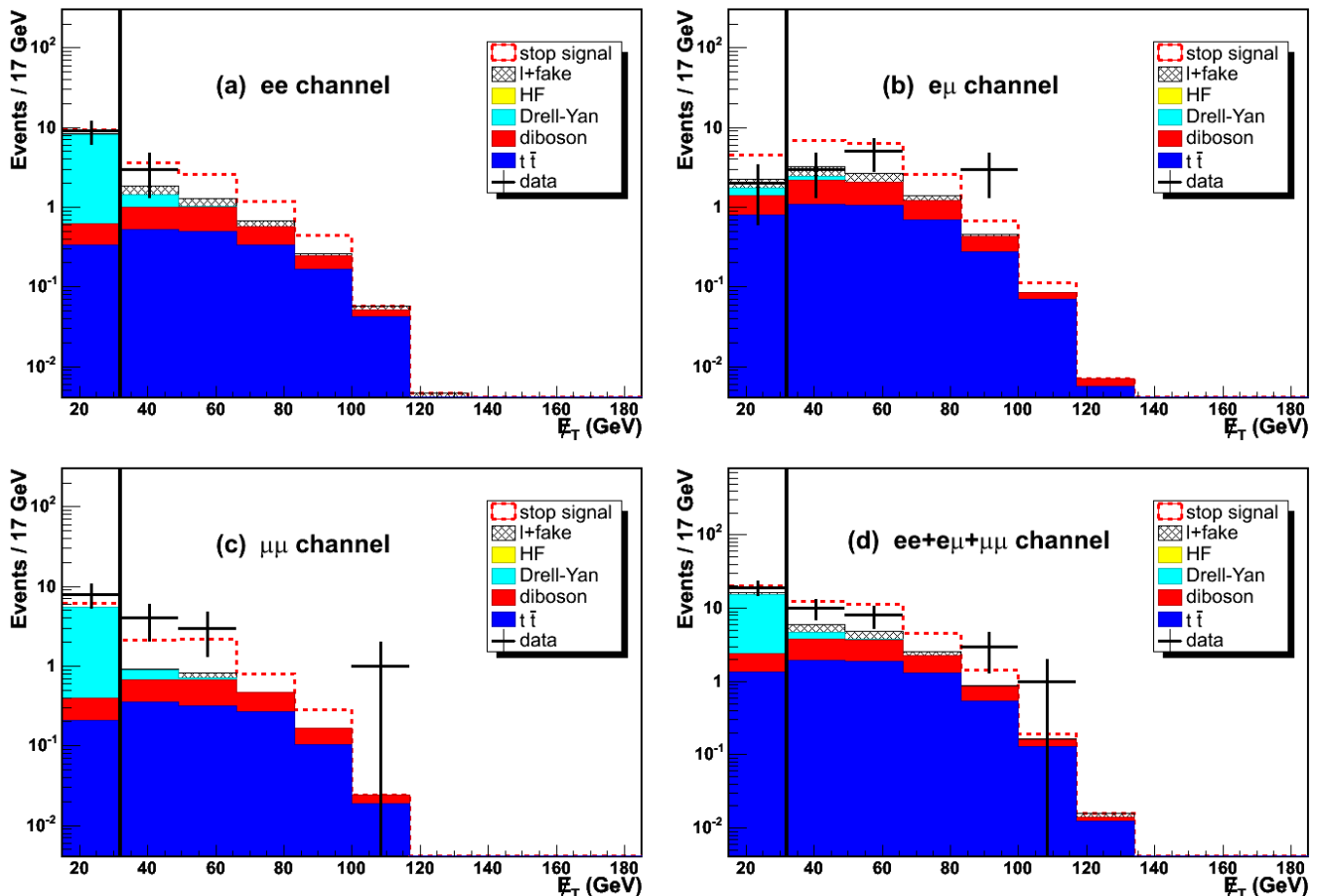


FIG. 5: The cut group $b \cancel{E}_T$ distributions for (a) the ee channel, (b) the $e\mu$ channel, (c) the $\mu\mu$ channel, and (d) the three channels combined with all other cuts applied. Data are shown as the points with error bars (statistical only). Shown as stacked histograms are the backgrounds arising from misidentified hadrons and decays-in-flight (l +fake), $b\bar{b}$ and $c\bar{c}$ (HF), DY, dibosons, and $t\bar{t}$. MC predictions for $(m_{\tilde{t}}, m_{\tilde{\nu}}) = (140, 90)$ GeV/ c^2 are stacked on top of the sums of backgrounds and are shown as the dashed line. The cut selects events to the right of the vertical line.

passing the above “inverse d_0 ” cuts. It is assumed that this scaling ratio is independent of dilepton mass in regions not dominated by Z boson decays. To estimate the heavy-flavor background, the resulting scaling factors, typically of order 2, are then applied to “inverse d_0 ” events passing cuts appropriate to the various control regions as well as the signal region. No heavy-flavor contribution to the signal region survives our final cuts.

IV. SIGNAL SAMPLES AND SYSTEMATIC UNCERTAINTIES

A total of 74 MC signal samples corresponding to values of $m_{\tilde{t}} = [55, 190]$ GeV/ c^2 and $m_{\tilde{\nu}} = [45, 110]$ GeV/ c^2 were generated using PYTHIA and the GEANT-based detector simulation. The events are scaled using the NLO PROSPINO cross section [16, 17] calculated with the CTEQ6M [18] parton distribution functions (PDFs). The cross sections depend on the stop quark mass and

	ee	$e\mu$	$\mu\mu$
DY	$72.8 \pm 4.8 \pm 26.3$	$26.6 \pm 2.7 \pm 5.4$	$62.4 \pm 4.1 \pm 28.4$
$t\bar{t}$	$6.1 \pm 0.1 \pm 0.7$	$13.1 \pm 0.1 \pm 1.4$	$4.2 \pm 0.1 \pm 0.5$
diboson	$3.5 \pm 0.1 \pm 0.6$	$6.2 \pm 0.1 \pm 1.1$	$2.1 \pm 0.0 \pm 0.4$
l +fake	$21.6 \pm 0.2 \pm 10.8$	$24.9 \pm 0.4 \pm 12.4$	$5.4 \pm 0.2 \pm 2.7$
HF	$9.1 \pm 4.1 \pm 7.4$	$30.6 \pm 7.9 \pm 10.5$	$8.5 \pm 4.3 \pm 6.7$
Total	$113 \pm 6 \pm 30$	$101 \pm 8 \pm 18$	$83 \pm 6 \pm 30$
Data	110	76	89

TABLE I: Expected backgrounds (DY, $t\bar{t}$, diboson, misidentified hadrons and decays-in-flight (l +fake), and $b\bar{b}$ and $c\bar{c}$ (HF)) and observed events in the pre-signal region. The first uncertainty listed is statistical and the second systematic. The systematic uncertainty includes a 6% uncertainty on the luminosity common to all entries.

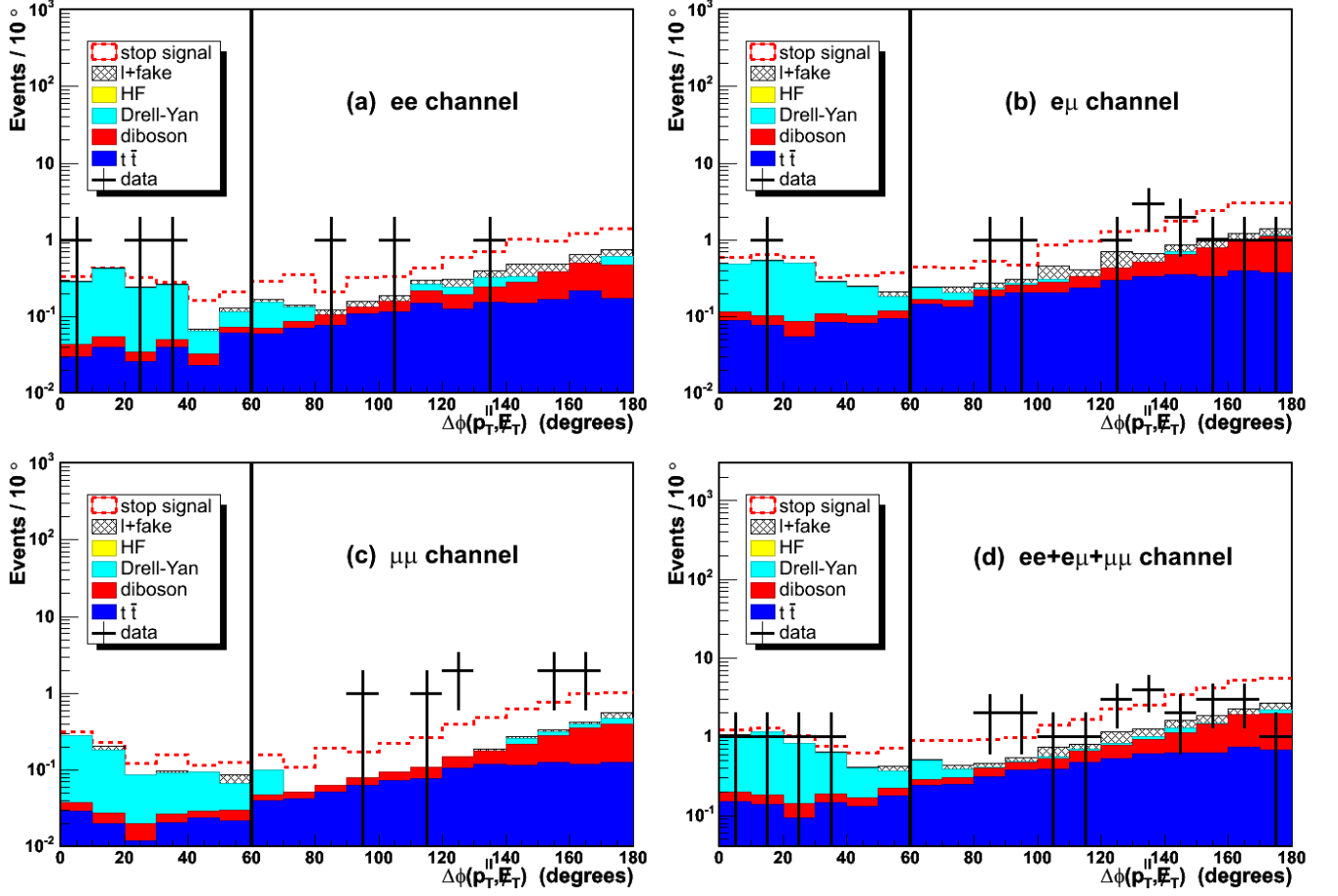


FIG. 6: The cut group b distributions of the absolute value of the azimuthal angle between the dilepton system and \cancel{E}_T , shown as in Fig. 5.

	ee	$\mu\mu$
DY	$12314 \pm 63 \pm 956$	$6904 \pm 43 \pm 568$
Data	12461	7111

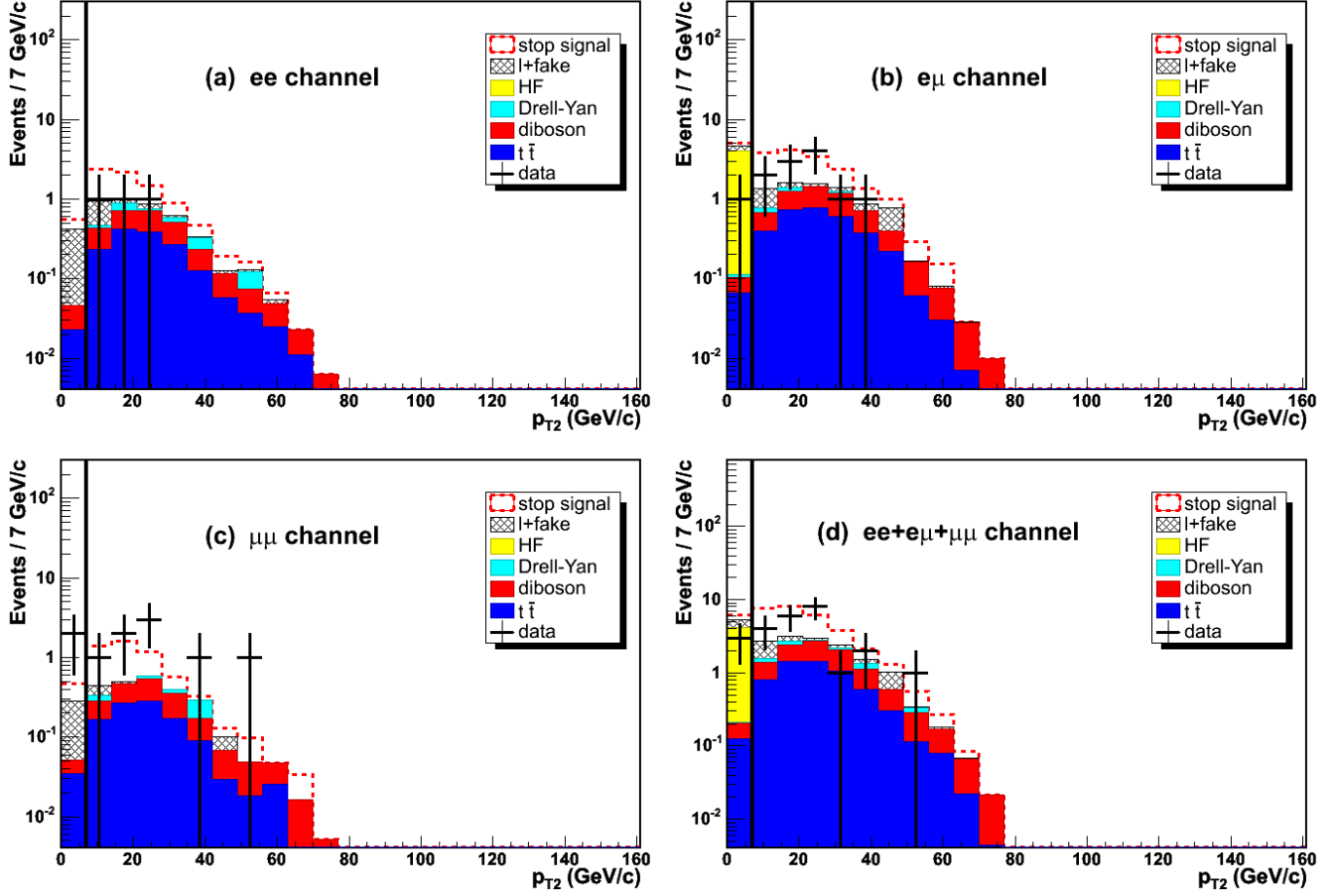
TABLE II: Expected DY background and observed events in the Z control region. The first uncertainty listed is statistical and the second systematic. The systematic uncertainty includes a 6% uncertainty on the luminosity common to both channels.

	ee	$e\mu$	$\mu\mu$
DY	$167 \pm 7 \pm 26$	$94 \pm 5 \pm 7$	$108 \pm 5 \pm 19$
$t\bar{t}$	$0.1 \pm 0.0 \pm 0.0$	$0.2 \pm 0.0 \pm 0.0$	-
diboson	$9.3 \pm 0.0 \pm 0.9$	$17.9 \pm 0.1 \pm 1.7$	$5.9 \pm 0.0 \pm 0.6$
e +fake	$23.1 \pm 0.1 \pm 11.5$	$11.8 \pm 0.3 \pm 5.9$	-
μ +fake	-	$14.8 \pm 0.1 \pm 7.4$	$4.7 \pm 0.2 \pm 2.4$
HF	$15.6 \pm 5.3 \pm 9.6$	$62.6 \pm 11.9 \pm 3.8$	$26.2 \pm 8.1 \pm 6.7$
Total	$215 \pm 9 \pm 30$	$202 \pm 13 \pm 13$	$145 \pm 10 \pm 20$
Data	186	167	114

only weakly, through higher-order corrections, on other SUSY parameters. Limits on the production cross section can therefore be translated into lower limits on the lightest stop quark mass without reference to other SUSY parameters. The branching ratio for the decay $\tilde{t} \rightarrow b l^+ \tilde{\nu}_l$, where $l = e, \mu$ or τ with equal probability, is assumed to be 100%.

There are several sources of systematic uncertainty on the background estimation. The systematic uncertainty due to the jet energy scale is determined by varying the jet energy corrections by $\pm 1\sigma$ [9]. The resulting uncertainty varies from less than 1% to 35% and is largest

TABLE III: Expected backgrounds (DY, $t\bar{t}$, diboson, misidentified hadrons and decays-in-flight (e +fake, μ +fake), and $b\bar{b}$ and $c\bar{c}$ (HF)) and observed events for the high- \cancel{E}_T / no jet control region. The first uncertainty listed is statistical and the second systematic. The systematic uncertainty includes a 6% uncertainty on the luminosity common to all entries.

FIG. 7: The cut group b p_{T2} distributions, shown as in Fig. 5.

	ee	$e\mu$	$\mu\mu$
DY	$6254 \pm 43 \pm 644$	$201 \pm 8 \pm 21$	$4681 \pm 35 \pm 526$
$t\bar{t}$	-	-	-
diboson	$1.4 \pm 0.0 \pm 0.1$	$2.5 \pm 0.0 \pm 0.2$	$0.8 \pm 0.0 \pm 0.1$
e +fake	$263 \pm 0 \pm 132$	$95 \pm 1 \pm 48$	-
μ +fake	-	$105 \pm 0 \pm 52$	$40 \pm 0 \pm 20$
HF	$826 \pm 86 \pm 138$	$1102 \pm 72 \pm 110$	$554 \pm 71 \pm 66$
Total	$7345 \pm 96 \pm 671$	$1505 \pm 72 \pm 132$	$5276 \pm 80 \pm 530$
Data	7448	1687	5344

TABLE IV: Expected backgrounds (DY, $t\bar{t}$, diboson, misidentified hadrons and decays-in-flight (e +fake, μ +fake), and $b\bar{b}$ and $c\bar{c}$ (HF)) and observed events for the low- \cancel{E}_T / no jet control region. The first uncertainty listed is statistical and the second systematic. The systematic uncertainty includes a 6% uncertainty on the luminosity common to all entries.

	ee	$e\mu$	$\mu\mu$
DY	$1161 \pm 19 \pm 223$	$42 \pm 3 \pm 6$	$1004 \pm 16 \pm 204$
$t\bar{t}$	$0.3 \pm 0.0 \pm 0.0$	$0.6 \pm 0.0 \pm 0.1$	$0.2 \pm 0.0 \pm 0.0$
diboson	$1.4 \pm 0.0 \pm 0.1$	$0.6 \pm 0.0 \pm 0.1$	$1.0 \pm 0.0 \pm 0.1$
e +fake	$215 \pm 0 \pm 107$	$61 \pm 1 \pm 31$	-
μ +fake	-	$94 \pm 0 \pm 47$	$28 \pm 0 \pm 14$
HF	$144 \pm 21 \pm 32$	$247 \pm 26 \pm 70$	$170 \pm 27 \pm 46$
Total	$1521 \pm 28 \pm 250$	$445 \pm 26 \pm 90$	$1204 \pm 32 \pm 209$
Data	1443	351	1246

TABLE V: Expected backgrounds (DY, $t\bar{t}$, diboson, misidentified hadrons and decays-in-flight (e +fake, μ +fake), and $b\bar{b}$ and $c\bar{c}$ (HF)) and observed events for the low- \cancel{E}_T / one or more jet control region. The first uncertainty listed is statistical and the second systematic. The systematic uncertainty includes a 6% uncertainty on the luminosity common to all entries.

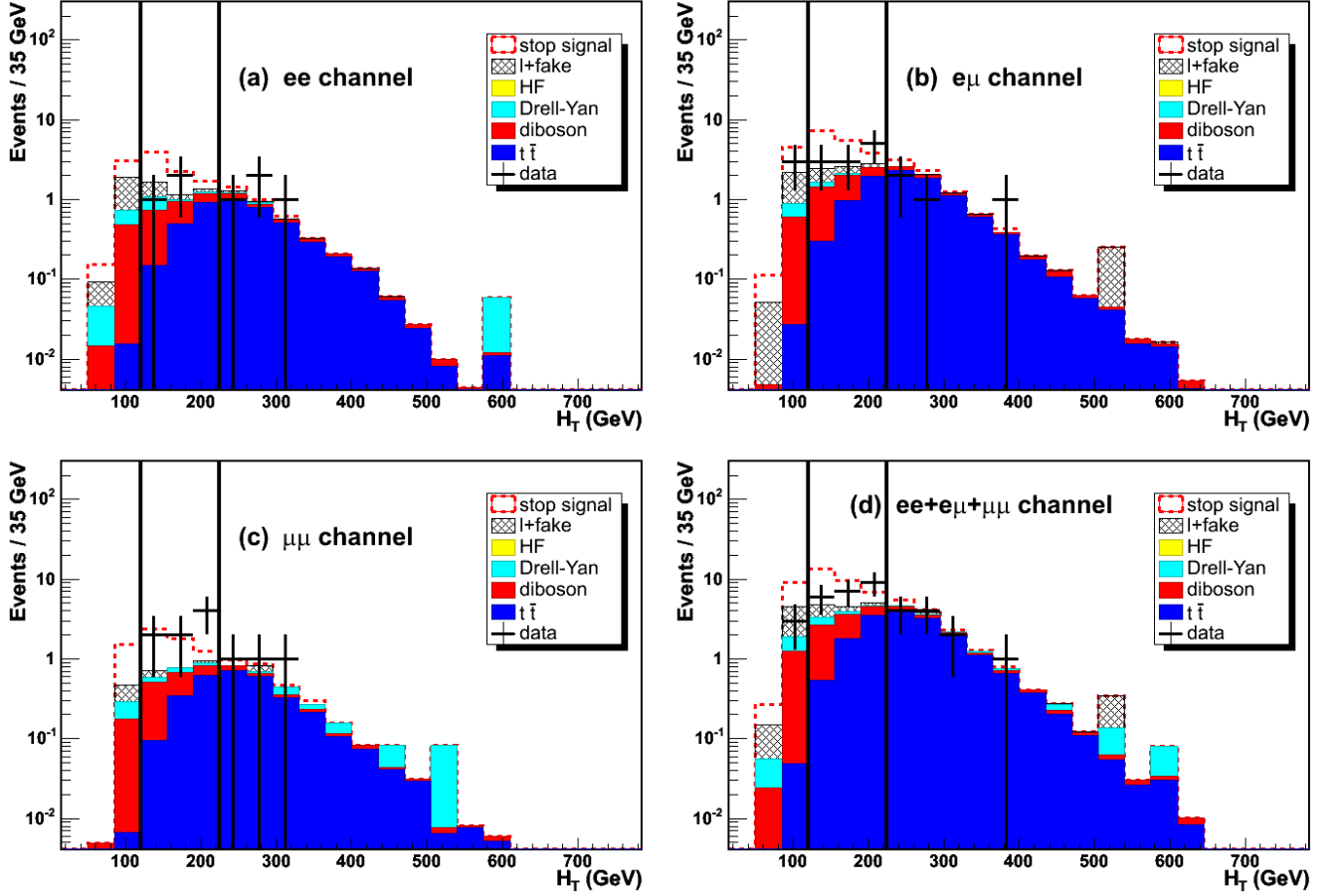


FIG. 8: The cut group b H_T distributions, shown as in Fig. 5. The cut selects events between the vertical lines.

Variable	Cut group			
	a	b	c	d
$\Delta m(\text{GeV}/c^2)$	5 – 47.5	47.5 – 72.5	72.5 – 87.5	> 87.5
\cancel{E}_T (GeV)	>25	>32	>32	>32
$\Delta\phi(p_T^l, \cancel{E}_T)$ (deg)	> 60	> 60	> 60	> 60
p_{T2} (GeV/ c)	>7	>7	>7	>7
H_T (GeV)	< 170	120 – 225	130 – 290	> 165
m_T (GeV/ c^2)	>15	>11	—	—
p_T^l (GeV/ c)	< $c\Delta m - 1$	—	—	—

TABLE VI: Table of cuts for the cut groups defining the four signal regions.

for DY events, which typically contain low- E_T jets. The uncertainty arising from ISR and FSR is determined by varying the parameters in PYTHIA that control the generation of ISR/FSR. The resulting uncertainty is $\simeq 3\%$. The uncertainty on the acceptance arising from the PDFs used in the MC is estimated using the uncertainties on the CTEQ eigenvectors and determined to be 2%. Other systematic uncertainties are: 6% on the measurement of the integrated luminosity, 2% on the dilepton trigger ef-

iciency, 2% on lepton identification efficiency, and 50% on the number of misidentified electrons and muons. The uncertainties on the cross sections used in the MC generation of the background are 8% for $t\bar{t}$, 2% for DY, 6% for WW , 8% for WZ , 10% for ZZ , and 7% for $W\gamma$.

The systematic uncertainties on the MC stop signal estimation are nearly identical to those on the background estimation. The uncertainty arising from the jet energy scale varies from 1% to 11% depending on the stop-sneutrino mass difference. The uncertainties due to ISR/FSR, PDFs, luminosity, trigger efficiency, and lepton identification are the same as for the background estimation.

V. INITIAL EVENT SELECTION AND CONTROL SAMPLES

We first define a pre-signal region by applying several event selection cuts to significantly reduce background and provide a data sample loosely consistent with the stop quark signature. We subsequently optimize additional cuts to improve the sensitivity of the search. This is done prior to revealing the contents of the data in

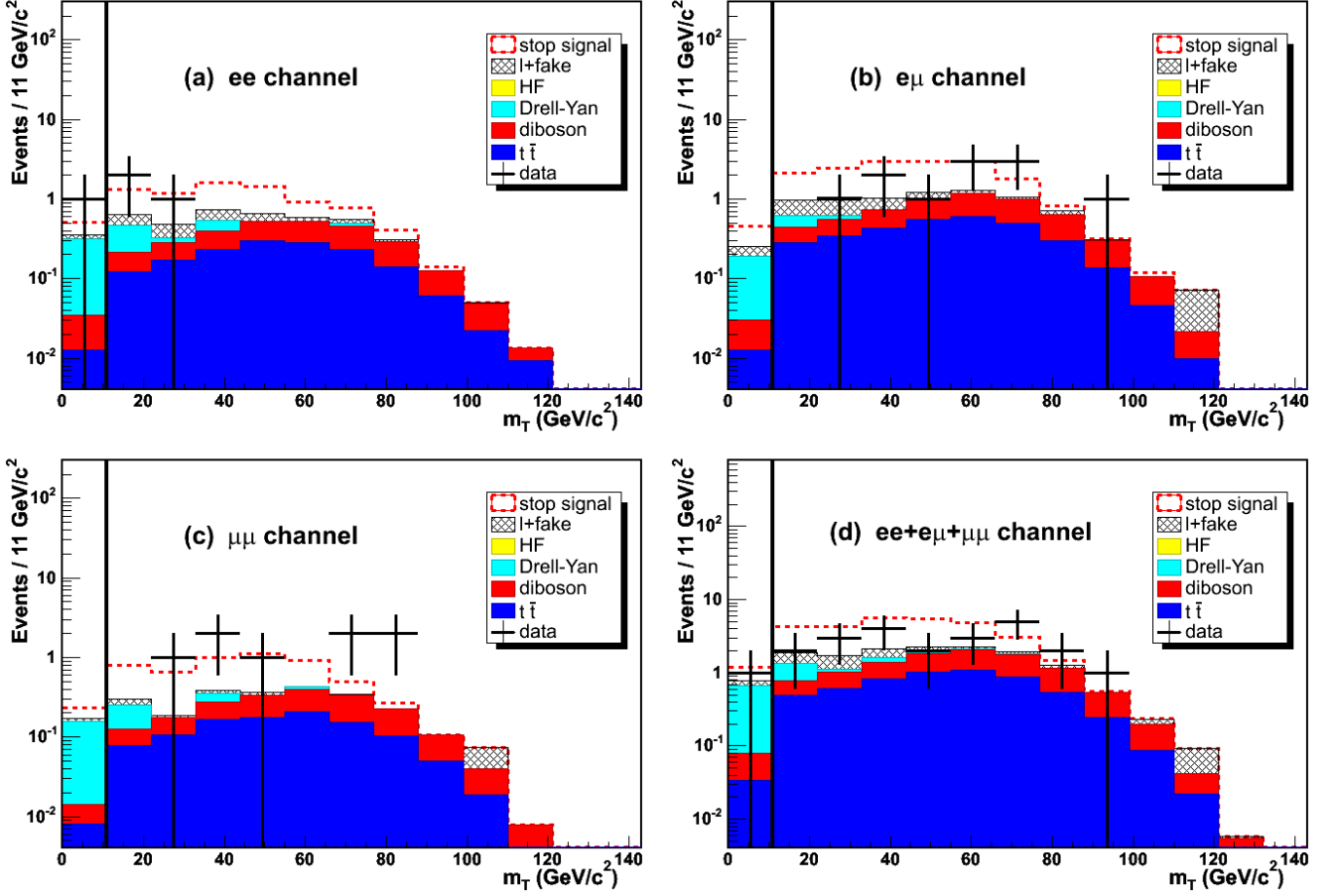


FIG. 9: The cut group b m_T distributions, shown as in Fig. 5.

the pre-signal region. At the pre-signal stage the following cut requirements are applied: two opposite-charge leptons, one with $p_T > 10$ GeV/ c and the other with $p_T > 5$ GeV/ c ; $m_{ll} > 15$ GeV/ c^2 , in order to remove sequential B -hadron decays and low mass resonances; $m_{ll} < 76$ GeV/ c^2 or $m_{ll} > 106$ GeV/ c^2 for same-flavor dilepton events, in order to eliminate Z boson events; at least one jet with corrected $E_T > 15$ GeV and $|\eta| < 2$; $\cancel{E}_T > 15$ GeV; $\Delta R(e, \text{highest-}E_T \text{ jet}) > 0.4$; $\Delta R(l, l) > 0.4$; and $\Delta\phi > 20^\circ$ between \cancel{E}_T and each of the leptons and the highest E_T jet.

Figure 1 shows the \cancel{E}_T distributions separately for ee , $e\mu$ and $\mu\mu$ events, as well as the summed distribution, in the pre-signal region. The expected \cancel{E}_T distribution for stop quark events with stop mass 150 GeV/ c^2 and sneutrino mass 75 GeV/ c^2 is also shown scaled up by a factor of five. Figures 2-4 show the corresponding plots for H_T , the p_T of the highest p_T lepton (p_{T1}), and the p_T of the next-to-highest p_T lepton (p_{T2}). H_T is defined as $H_T = \cancel{E}_T + p_{T1} + p_{T2} + E_{Tj}$, where E_{Tj} is the transverse energy of the highest p_T jet. Table I lists the sources of expected background for the pre-signal region and the number of observed events. Good agreement of data with the background estimations is observed.

To check the accuracy of our estimation of SM backgrounds, a number of “control regions” are defined. One control region consists of same-flavor, opposite-charge lepton events with invariant mass $76 < m_{ll} < 106$ GeV/ c^2 (the Z region). No jet or \cancel{E}_T requirements are imposed. The background is expected to arise almost entirely from DY processes. Table II gives the number of observed events in the Z region and the expected background. Good agreement is seen, demonstrating accurate modeling of the predominantly DY background.

Another control region consists of events where we require $\cancel{E}_T > 15$ GeV and no jets with $E_T > 15$ GeV. All the other pre-signal cuts are applied except for the $\Delta\phi > 20^\circ$ cut between \cancel{E}_T and each of the two highest p_T leptons and the highest E_T jet. This control region predominantly tests the modeling of the high \cancel{E}_T tail of DY and HF events. Table III gives a breakdown of the expected backgrounds and the number of observed events for this control region. Reasonable agreement is observed between the expected background and data. The significant number of $e\mu$ DY events (comparable to the number of ee and $\mu\mu$ events) is due to $Z \rightarrow \tau\tau$ decays where one τ subsequently decays to an electron and the other to a muon.

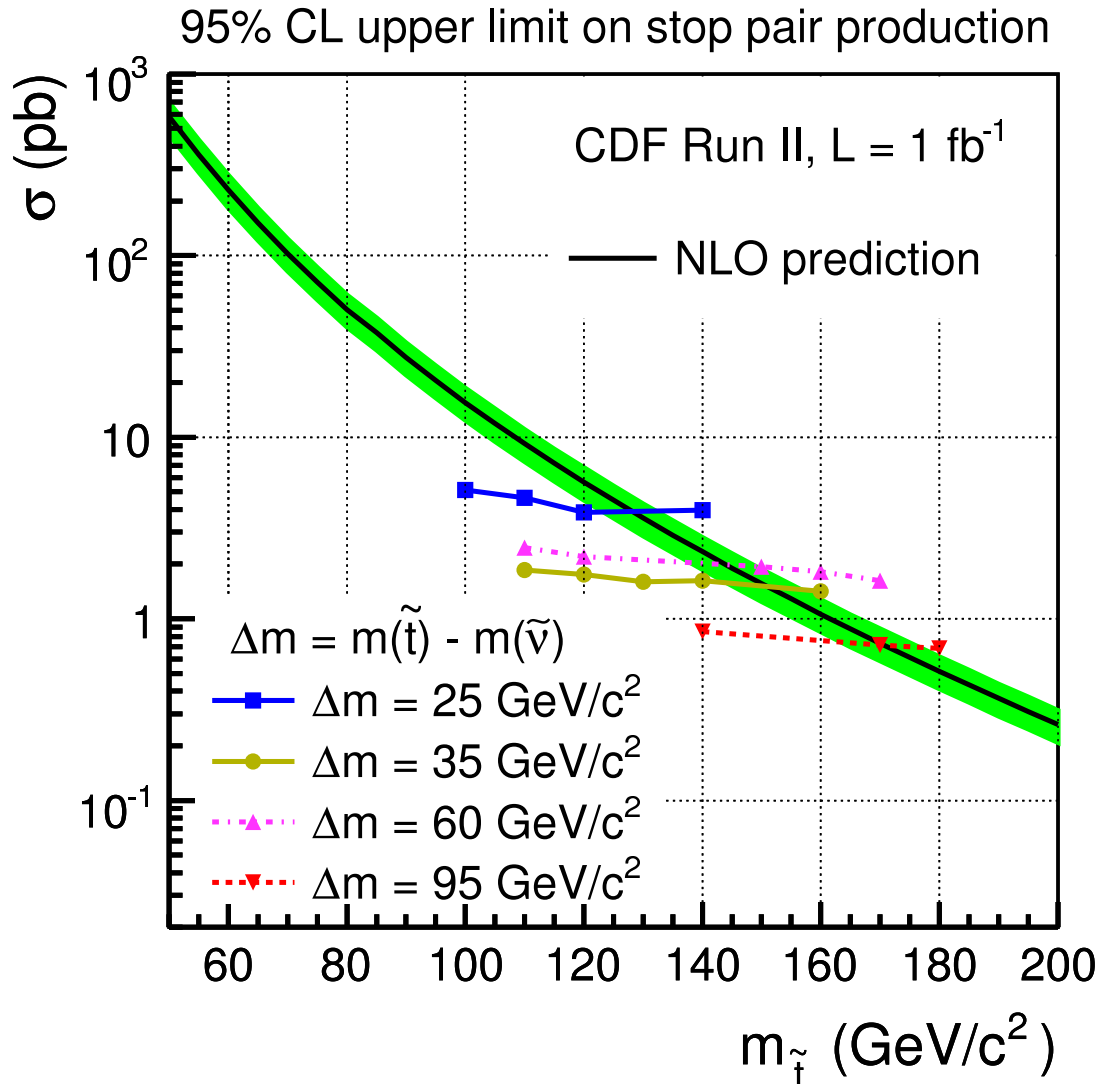


FIG. 10: Stop cross section upper limits for fixed stop-sneutrino mass differences. The NLO PROSPINO cross section with CTEQ6M PDFs is shown as the solid curve. The band represents the theoretical uncertainty in the cross section due to uncertainties on the renormalization and factorization scales and the PDFs.

Two additional control regions are defined as having $\cancel{E}_T < 15 \text{ GeV}$ and either the presence or absence of jets with $E_T > 15 \text{ GeV}$. These control regions are sensitive to the modeling of heavy flavor and the photon component of DY. All other cuts are the same as for the previous control region. Tables IV and V list the expected backgrounds and the number of observed events for these control regions. In both cases, the data agree well with the expected backgrounds.

VI. OPTIMIZATION OF CUTS

The signal regions are determined by optimizing cuts on variables that minimize the limit on the $\tilde{t}\tilde{t}^*$ production cross section determined with Bayesian meth-

ods [19]. The $ee, e\mu,$ and $\mu\mu$ final states are tuned simultaneously and flavor-independent cut values are obtained. The most useful variables for discriminating stop quark signal from background are: \cancel{E}_T ; H_T ; the absolute value of the difference in azimuthal angle between the dilepton system and \cancel{E}_T ; p_{T2} ; the transverse momentum of the dilepton system (p_T^l); and the transverse mass between each lepton (l) and \cancel{E}_T , defined as $m_{Tl} = \sqrt{2p_{Tl}\cancel{E}_T[1 - \cos(\Delta\phi(l, \cancel{E}_T))]}$ where the index l labels the lepton.

The optimum values for the cut variables depend on the mass difference ($\Delta m = m_{\tilde{t}} - m_{\tilde{\nu}}$) which we group into four sets labeled a through d in Δm bands parallel to and below the $m_{\tilde{t}} = m_{\tilde{\nu}} + m_b$ kinematic limit. Four cut groups were chosen as a compromise between having the cuts near their optimal values for each stop-sneutrino point

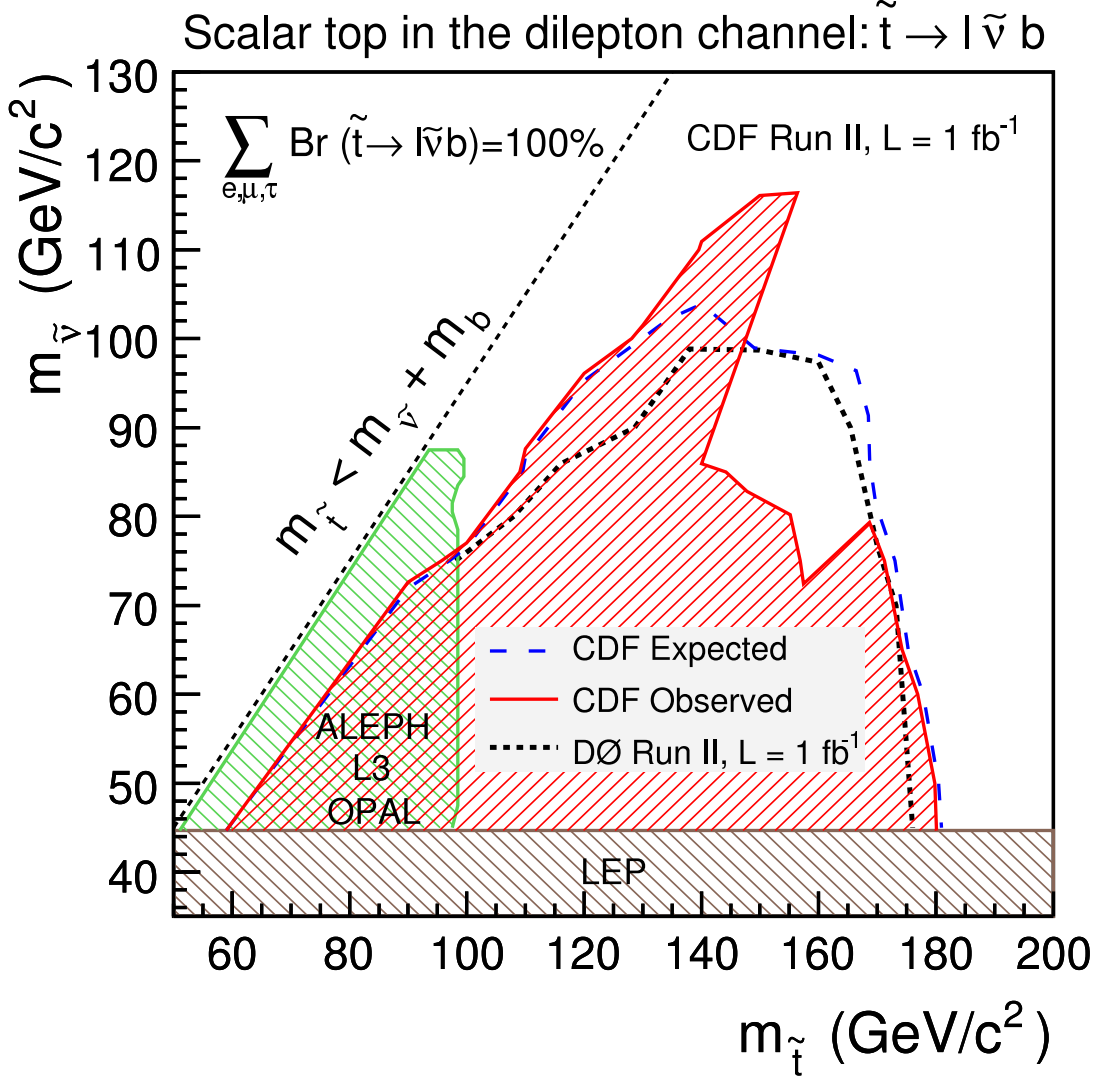


FIG. 11: Observed and expected limits in the stop-sneutrino mass plane. The LEP limits are for a mixing angle of zero which provides the greatest reach.

while keeping the number of cut groups to a minimum. The definitions of the four cut groups and the values of the cuts used are given in Table VI.

The \cancel{E}_T distributions for the signal region are shown in Fig. 5 for cut group *b*, where the other cuts listed in Table VI are all applied. The individual backgrounds are shown as well as the data. For reference the expected signal from the stop-sneutrino mass point (140,90) GeV/c² is also shown added to the stacked backgrounds. The vertical line represents the lower bound placed on \cancel{E}_T for this cut group. The \cancel{E}_T cut is the most effective at reducing the DY, $b\bar{b}$ and $c\bar{c}$, and l +fake backgrounds. In particular, the DY background is expected to show a small energy imbalance in the detector, while the reference-point signal events are characterized by large energy imbalance. The cut on \cancel{E}_T reduces the DY background by more than a factor of 10 even when all other final cuts have been

applied, while reducing the expected signal by only 20%.

As shown in Fig. 6, the cut on the absolute value of the azimuthal angle between the dilepton system and \cancel{E}_T is useful in further suppressing the dominant DY background. This cut discriminates against DY events where the \cancel{E}_T arises from mismeasurement of the leptons or from $\tau\tau$ events where neutrinos from the τ decay result in \cancel{E}_T aligned with the leptons coming from the decay.

Leptons arising from stop quark decay are typically more energetic than those coming from *b* or *c* quark decay because of the higher stop quark mass. A cut on p_{T2} , whose distribution is shown in Fig. 7, removes all the $b\bar{b}$ and $c\bar{c}$ background remaining after the other cuts have been applied. Only 5% of the reference-point signal events are removed by this cut.

The $t\bar{t}$ background is especially difficult to reduce without severely impacting the efficiency for stop quark detec-

cut group	flavor	DY	$t\bar{t}$	diboson	l +fake	Total Background	$t\bar{t}$	Data
<i>a</i>	ee	0.9±0.4	0.1±0.0	0.5±0.1	1.7±0.9	3.3±0.9	3.2±0.5	1
	$e\mu$	0.3±0.1	0.3±0.0	1.0±0.2	2.0±1.0	3.6±1.0	6.6±0.8	2
	$\mu\mu$	0.6±0.4	0.1±0.0	0.3±0.1	0.2±0.1	1.1±0.4	2.9±0.4	1
	$ee + e\mu + \mu\mu$	1.8±0.7	0.5±0.1	1.8±0.3	3.9±1.7	7.9±1.9	12.8±1.4	4
<i>b</i>	ee	0.5±0.3	1.6±0.2	1.3±0.2	1.6±0.8	4.9±0.9	3.7±0.4	3
	$e\mu$	0.3±0.1	3.2±0.3	2.8±0.5	2.5±1.3	8.7±1.4	8.8±0.8	11
	$\mu\mu$	0.3±0.1	1.1±0.1	1.0±0.2	0.2±0.1	2.4±0.3	3.0±0.4	8
	$ee + e\mu + \mu\mu$	1.0±0.4	5.8±0.6	5.0±0.9	4.3±1.8	16.1±2.3	15.6±1.4	22
<i>c</i>	ee	0.8±0.4	3.3±0.4	1.4±0.2	1.3±0.6	6.7±0.8	6.1±0.5	7
	$e\mu$	0.3±0.1	7.1±0.8	2.9±0.5	2.1±1.1	12.5±1.4	12.6±0.9	13
	$\mu\mu$	0.4±0.2	2.3±0.3	1.0±0.2	0.2±0.1	3.9±0.4	4.2±0.4	9
	$ee + e\mu + \mu\mu$	1.5±0.5	12.7±1.4	5.3±0.9	3.6±1.5	23.1±2.6	22.9±1.6	29
<i>d</i>	ee	0.4±0.1	4.4±0.5	0.9±0.2	0.6±0.3	6.2±0.6	3.4±0.3	5
	$e\mu$	0.1±0.0	9.4±1.0	1.9±0.3	1.4±0.7	12.7±1.3	7.3±0.5	11
	$\mu\mu$	0.5±0.2	3.0±0.4	0.7±0.1	0.2±0.1	4.4±0.5	2.3±0.2	8
	$ee + e\mu + \mu\mu$	1.0±0.4	16.8±1.8	3.5±0.6	2.1±0.9	23.3±2.4	13.0±0.9	24

TABLE VII: Expected backgrounds and observed events for cut groups $a - d$. The uncertainties represent the statistical and systematic uncertainties added in quadrature. The systematic uncertainty includes a 6% uncertainty on the luminosity common to all entries. Also shown are the number of expected $t\bar{t}$ events for (stop, sneutrino) masses (130,95), (140,90), (150,75), and (180,50) GeV/ c^2 in cut groups a, b, c and d respectively.

tion. However, because the sneutrino carries a significant fraction of the available energy, the remaining stop quark decay products typically have less energy than their counterparts from top quark decay. As a result the H_T distribution, as shown in Fig. 8, peaks at lower values for stop quarks than for top quarks. An upper limit on H_T is effective at reducing the amount of $t\bar{t}$ background while a lower limit helps reduce the other backgrounds.

A transverse mass cut is used in the low Δm cut groups (a and b) to remove most of the DY background remaining after the other cuts have been applied. The transverse mass distribution for cut group b is shown in Fig. 9.

The upper bound on the transverse momentum of the dilepton system is applied to the lowest Δm cut group (a) to reduce the $t\bar{t}$ and diboson backgrounds. Its effectiveness decreases as Δm increases. The sliding cut is determined by a linear fit to the optimal dilepton p_T values as a function of Δm in cut group a : $p_T^H < (c\Delta m - 1)$ GeV/ c .

VII. RESULTS AND CONCLUSIONS

The numbers of expected background and observed data events for cut groups $a - d$ are given in Table VII. In general the agreement between data and SM background estimations is good, although the statistical uncertainties are large. The largest deviation is an excess of data over background expectations for $\mu\mu$ events with large \cancel{E}_T . Examination of individual event properties found no evidence for cosmic rays or pion or kaon decays-in-flight. These results are not independent observations, since there is a large overlap in events between cut groups b, c , and d . The largest muon excess, found in cut group

b , has a 0.4% probability for the modeled background to fluctuate up to the number of observed events or more (p-value), when considering this cut group alone. The p-value includes the effects of the estimated background uncertainty. Combining all channels in cut group b raises the probability to 12.4%. The corresponding one-sided Gaussian significances are 2.6 σ and 1.2 σ respectively.

A joint likelihood is formed from the product of the individual channel likelihoods. Using this likelihood, we apply a Bayesian method [19] with a flat prior for the signal to set 95% confidence level upper limits on the production cross section at each considered point in the stop-sneutrino mass plane. Systematic uncertainties are incorporated by convolving the Poisson probabilities for the signal with Gaussian distributions representing each background uncertainty. The three dilepton flavor channels are incorporated into the statistical analysis simultaneously (but individually), with full treatment of correlated and uncorrelated uncertainties. The correlations between the various backgrounds and the MC-generated signal are also accounted for.

One-dimensional curves of the upper cross section limits and the theoretical cross section are shown in Fig. 10 for groups of points with fixed Δm . The cross section upper limits for a given Δm tend to be almost independent of the stop mass.

To determine the observed (expected) exclusion contour in the stop-sneutrino mass plane, we set the number of events equal to the number of events in the data (total expected background). We then calculate the 95% confidence level upper limits on the stop pair cross section for 74 points in the $(m_{\tilde{t}}, m_{\tilde{\nu}})$ plane to determine both the points we exclude and those that we expect to exclude in the absence of signal. We interpolate linearly

between nearby excluded and not-excluded points. The expected and observed limits are shown in Fig. 11 along with previous limits [4, 5].

In conclusion, this analysis extends the previously existing exclusion limits to higher sneutrino masses for stop masses in the range 135-155 GeV/ c^2 , and to stop masses up to 180 GeV/ c^2 , for low sneutrino masses. For a particular set of optimization cuts (cut group b), a 2.6 σ excess of $\mu\mu$ events is observed, but is reduced to 1.2 σ when all channels are combined.

VIII. ACKNOWLEDGMENTS

We thank the Fermilab staff and the technical staffs of the participating institutions for their vital contributions. This work was supported by the U.S. Department

of Energy and National Science Foundation; the Italian Istituto Nazionale di Fisica Nucleare; the Ministry of Education, Culture, Sports, Science and Technology of Japan; the Natural Sciences and Engineering Research Council of Canada; the National Science Council of the Republic of China; the Swiss National Science Foundation; the A.P. Sloan Foundation; the Bundesministerium für Bildung und Forschung, Germany; the World Class University Program, the National Research Foundation of Korea; the Science and Technology Facilities Council and the Royal Society, UK; the Institut National de Physique Nucleaire et Physique des Particules/CNRS; the Russian Foundation for Basic Research; the Ministerio de Ciencia e Innovación, and Programa Consolider-Ingenio 2010, Spain; the Slovak R&D Agency; and the Academy of Finland.

-
- [1] H. P. Nilles, Phys. Rep. **110**, 1 (1984); H. E. Haber and G. L. Kane, Phys. Rep. **117**, 75 (1985).
- [2] J. Ellis and S. Rudaz, Phys. Lett. B **128**, 248 (1983); K. I. Hikasa and M. Kobayashi, Phys. Rev. D **36**, 724 (1987); M. Drees and K. Hikasa, Phys. Lett. B **252**, 127 (1990).
- [3] W. Beenakker, M. Krämer, T. Plehn, M. Spira, and P. M. Zerwas, Nucl. Phys. B **515**, 3 (1998).
- [4] LEPSUSYWG, ALEPH, DELPHI, L3 and OPAL experiments, note LEPSUSYWG/04-01.1; note LEPSUSYWG/04-02.1; note LEPSUSYWG/01-03.1 (<http://lepsusy.web.cern.ch/lepsusy/Welcome.html>).
- [5] T. Affolder *et al.* (CDF Collaboration), Phys. Rev Lett. **84**, 5273 (2000); T. Affolder *et al.* (CDF Collaboration), Phys. Rev Lett. **84**, 5704 (2000); V. M. Abazov *et al.* (D0 Collaboration), Phys. Rev. Lett. **88**, 171802 (2002); D. Acosta *et al.* (CDF Collaboration), Phys. Rev Lett. **90**, 251801 (2003); V. M. Abazov *et al.* (D0 Collaboration), Phys. Rev. Lett. **93**, 011801 (2004); T. Aaltonen *et al.* (CDF Collaboration), Phys. Rev. D **76**, 072010 (2007); V. M. Abazov *et al.* (D0 Collaboration), Phys. Lett. B **645**, 119 (2007); V. M. Abazov *et al.* (D0 Collaboration), Phys. Lett. B **659**, 500 (2008); V. M. Abazov *et al.* (D0 Collaboration), Phys. Lett. B **675**, 289 (2009).
- [6] CDF uses a cylindrical coordinate system in which ϕ is the azimuthal angle, r is the radius from the nominal beam line, and z points in the proton beam direction. The transverse ($r - \phi$) plane is perpendicular to the z axis. Transverse momentum and energy are the respective projections of momentum measured in the tracking system and energy measured in the calorimeter system onto the $r - \phi$ plane, and are defined as $p_T = p \sin \theta$ and $E_T = E \sin \theta$. Here, θ is the polar angle measured with respect to the interaction vertex. Missing transverse energy (\vec{E}_T) is defined by $\vec{E}_T = -\sum_i E_T^i \vec{n}_i$, where i is the calorimeter tower and \vec{n}_i is a unit vector perpendicular to the beam axis and pointing at the i th tower. The pseudorapidity η is defined as $-\ln(\tan(\theta/2))$, where θ is measured with respect to the origin of the detector. We define the magnitude $E_T = |\vec{E}_T|$.
- [7] F. Abe *et al.*, Nucl. Instrum. Methods Phys. Res. A **271**, 387 (1988); D. Amidei *et al.*, Nucl. Instrum. Methods Phys. Res. A **350**, 73 (1994); F. Abe *et al.*, Phys. Rev. D **52**, 4784 (1995); P. Azzi *et al.*, Nucl. Instrum. Methods Phys. Res. A **360**, 137 (1995); The CDFII Detector Technical Design Report, Fermilab-Pub-96/390-E; A. Abulencia *et al.*, J. Phys. G Nucl. Part. Phys. **34**, 2457 (2007).
- [8] D. Acosta *et al.*, Phys. Rev. D **72**, 052003 (2005); T. Aaltonen *et al.*, Phys. Rev. D **79**, 052004 (2009).
- [9] A. Bhatti *et al.*, Nucl. Instrum. Methods Phys. Res. A **566**, 375 (2006).
- [10] T. Sjöstrand, L. Lönnblad and S. Mrenna, J. High Energy Phys. **05**, 026 (2006). PYTHIA version 6.126 was used in this analysis.
- [11] S. Agostinelli *et al.*, Nucl. Instrum. Methods Phys. Res. A **506**, 250 (2003); J. Allison *et al.*, IEEE Trans. Nucl. Sci. **1**, 270 (2006).
- [12] M. Cacciari *et al.*, J. High Energy Phys. **04**, 068 (2004).
- [13] F. Abe *et al.*, Phys. Rev. D **59**, 052002 (1999).
- [14] J. M. Campbell and R. K. Ellis, Phys. Rev. D **60**, 113006 (1999); S. Eidelman *et al.* (Particle Data Group), Phys. Lett. B **592**, 1 (2004).
- [15] U. Baur and E. L. Berger, Phys. Rev. D **41**, 1476 (1990); U. Baur, T. Han, and J. Ohnemus, Phys. Rev. D **48**, 5140 (1993).
- [16] W. Beenakker, R. Höpker, M. Spira, and P. M. Zerwas, Nucl. Phys. B **492**, 51 (1997).
- [17] W. Beenakker, R. Höpker, and M. Spira, arXiv:hep-ph/9611232v1. PROSPINO version 2 was used in this analysis.
- [18] J. Pumplin, D.R. Stump, J. Huston, H.L. Lai, P. Nadolsky, and W.K. Tung, J. High Energy Phys. **07**, 012 (2002); D. Stump, J. Huston, J. Pumplin, W.K. Tung, H.L. Lai, S. Kuhlmann, and J.F. Owens, J. High Energy Phys. **10**, 046 (2003).
- [19] J. Conway, CERN Report No. 2000-005, 2000, p.247.